Superior efficiency of BN/Ce2O3/TiO2 nanofibers for photocatalytic hydrogen generation reactions

Massomeh Ghorbanloo, Amr Nada, Heba El-Maghrabi, Maged Bekheet, Wiebke Riedel, Bezzerga Djamel, Roman Viter, Stéphanie Roualdès, Fathi Soliman, Yasser Moustafa, et al.

To cite this version:

Massomeh Ghorbanloo, Amr Nada, Heba El-Maghrabi, Maged Bekheet, Wiebke Riedel, et al.. Superior efficiency of BN/Ce2O3/TiO2 nanofibers for photocatalytic hydrogen generation reactions. Applied Surface Science, 2022, 594, pp.153438. 10.1016/j.apsusc.2022.153438 . hal-03715516

HAL Id: hal-03715516
https://hal.science/hal-03715516

Submitted on 6 Jul 2022

Superior efficiency of BN/Ce_2O_3/TiO_2 nanofibers for photocatalytic hydrogen generation reactions

Massomeh Ghorbanloo [a,b,*] , Amr A. Nada [a,c,*], Heba H. El-Maghrabi [a,d], Maged F. Bekheet [e], Wiebke Riedel [f], Bezzerga Djamel [g], Roman Viter [h,i], Stéphanie Roualdes [a], Fathi S. Soliman [d], Yasser M. Moustafa [c], Philippe Miele [a], Mikhael Bechelany [a,*]

[a] Institut Européen des Membranes, IEM, UMR 5635, Univ Montpellier, ENSCM, CNRS, Montpellier, France

[b] Chemistry Department, Faculty of Science, University of Zanjan, Zanjan, Iran.

[c] Department of Analysis and Evaluation, Egyptian Petroleum Research Institute, Cairo 11727, Egypt

[d] Department of Refining, Egyptian Petroleum Research Institute, Cairo 11727, Egypt.

[e] Fachgebiet Keramische Werkstoffe/Chair of Advanced Ceramic Materials, Institut für Werkstoffwissenschaften und -technologien, Technische Universität Berlin, Hardenbergstraße 40, 10623 Berlin, Germany

[f] Institut für Chemie, Freie Universität Berlin, Arnimallee 22, 14195 Berlin, Germany

[g] Département de Physique, Institut de Sciences de la nature et de vie & Sciences exactes (SNV-SE), Universitaire of Relizane, Relizane, 48000, Algeria

[h] Institute of Atomic Physics and Spectroscopy, University of Latvia, 19 Raina Blvd., LV 1586 Riga, Latvia

[i] Sumy State University, Center for Collective Use of Scientific Equipment 31, Sanatornaya st., 40018 Sumy, Ukraine

* Corresponding author: m_ghorbanloo@yahoo.com, chem_amr@yahoo.com & mikhael.bechelany@umontpellier.fr

Abstract

One-dimensional BN/Ce_2O_3/TiO_2 heteroarchitectures with high visible-light photocatalytic activity have been successfully obtained by an electrospinning technique. The properties of the prepared nanofibers were controlled using different ratios of cerium. The results of XPS characterization revealed that the Ce element is present in the valence state +III on the surface of the TiO_2 nanofibers. Rietveld refinement of XRD data reveals that introducing small concentrations of Ce^{3+} (1-<3.0 at%) into the electrospinning solution leads to the formation of small amounts of rutile and brookite phases, a decrease in the crystallite size of the main anatase phase and a slight decrease in the *c* parameter and unit cell volume of the anatase phase. In contrast, only the anatase phase, which has a similar crystallite size and lattice parameters to that formed in the undoped sample, is observed when 3 at.% Ce is used. These results suggest that Ce^{3+} ions did not substitute Ti^{4+} ions in the lattice of both anatase and rutile phases, which can be explained by the large difference in the ionic radius of Ti^{4+} and Ce^{3+} ((r (Ti^{4+}) = 60.5 pm, r (Ce^{3+}) = 101.7 pm. Scanning electron microscopy demonstrates that the diameter of the obtained nanofibers decreases from 240 nm for pristine TiO_2 to 101 nm, 70 nm, 40 nm for CET2, BT and BCET2, respectively. The d-spacing decreased by 0.3 nm after Ce incorporation as demonstrated by high-resolution transmission electron microscopy. XPS proved the presence of BN nanosheets along with Ce_2O_3 and TiO_2 into the nanofibers. Compared with the pure TiO_2 nanofibers (NF), the obtained Ce/Ti ratio of 2% (molar ratio) showed an enhancement of the visible-light photocatalytic activity to water splitting, which is 46 times higher than that of bare TiO_2 NF. The Ce_2O_3 might improve the separation of photogenerated electrons and holes derived from the coupling effect of TiO_2 and cerium oxide. This work also examines the modification of TiO_2 (anatase) properties with hexagonal boron nitride (*h*-BN) and the impact this coupling has on photocatalytic activity. XPS proved the presence of BN nanosheets along with Ce_2O_3 and TiO_2 into the nanofibers. The electron transfer rate was improved by BN exfoliation. The photocatalytic results indicated that the $BN/Ce_2O_3/TiO_2$ nanofibers improve hydrogen production up to 5100 μmol/g for 6 h under visible light, which could be due to the presence of BN sheets that enhanced the separation of the photo-induced electron–hole pairs in TiO_2 and increased the specific surface area compared to pure TiO_2 and Ce_2O_3/TiO_2 nanofibers. Moreover, the $BN/Ce_2O_3/TiO_2$ could be easily recycled without decrease in the photocatalytic activity because of its one-dimensional nanostructure nature. Moreover, the present work focuses on the ternary composite of $BN/Ce_2O_3/TiO_2$ for optimization of electronic and phonon transport properties using the state-of-the-art density functional theory (DFT). The calculated electronic density of states (DOS) modulus shows an excellent agreement compared with available theoretical and experimental data for hydrogen production.

Keywords: Ce_2O_3/TiO_2 nanocomposite ; Electrospinning; Rare earth metal; Hydrogen evolution; reusability;

Introduction

Demand for clean and renewable energy resources as an alternative to conventional energy sources such as fossil fuels is increasing. Hydrogen gas has been introduced in recent years as a unique, clean energy resource [1-4]. H_2 has a high gravimetric energy density (142 MJ/kg), its combustion is environmentally friendly and it can be readily stored. However, hydrogen generation *via* renewable processes is still a concern [5, 6].

Photocatalytic water splitting is an artificial photocatalytic process that converts the sunlight into clean and renewable hydrogen fuel by decomposing water into its components, namely dihydrogen and dioxygen [7]. The process implies a catalyst, a visible-light absorbing material, and an electron donor. So far, a wide range of semiconductors has been used as photocatalysts. Among them, the anatase polymorph of TiO_2 has attracted significant attention due to its excellent chemical stability, low cost, and non-toxicity [8-10]. Despite the advantages of TiO_2, it has not yet found practical applications due to the undesired recombination of photo-excited carriers and its high bandgap, the latter being particularly not compatible with visible light. In this respect, many efforts have been carried out to modify the physical and chemical properties of TiO_2 to enhance its photosensitivity to visible light, such as increasing the crystallinity of TiO_2, loading TiO_2 with cations, coupling TiO_2 with other semiconductors, and adding sacrificial reagents to the reaction solution [8, 10].

It is believed that the crystallinity and morphology of TiO_2 govern its photocatalytic performance. In fact, the crystallinity of TiO_2 greatly affects its solar energy absorption features, reaction kinetics as well as charge carriers separation [11]. This is because the semiconductor alignment, electronic structure, and ease of reactants binding, change with the morphology of the TiO_2 surface. Among different morphologies reported for TiO_2, one-dimensional (1D) nanofibers (NFs) have gained attention due to their application in electronic and optoelectronic devices and their unique functional properties such as semi-directed charge transport, enhanced charge carriers mobility, and large surface area [12]. The high photocatalytic activity of TiO_2 NFs is assigned to their mesoporosity as well as to the alignment of nanoparticles in the crystalline material, which facilitates an effective charge separation by inter-particles charge transfer through the nanofiber framework [13]. 1D NFs can be fabricated through the electrospinning technique. This technique is particularly useful since it has a high throughput in a continuous process and under mild conditions [14]. Furthermore, catalysts on the resulting electrospun nanofibers can be simply recovered and reused, making them economically advantageous and environmentally friendly. Therefore, catalysts prepared by this method have been identified as green catalysts [15].

The photocatalytic activity of TiO_2 can also be enhanced by the incorporation of different metal ions [16]. The structural defects of the coupled TiO_2 (e.g., oxygen vacancies) can increase or decrease depending on the oxidation state and ionic radius of the guest element. Typically, lower valency metal dopants induce more oxygen vacancies in the structure of TiO_2 for charge compensation. These vacancies do not only narrow the spectroscopic bandgap, but also trap the carriers temporarily [17]. In the present work, we use the *4f* metal ion, Ce^{+3}, because of its superior mixed Ce^{3+}/Ce^{4+} states and great efficiency of the electron trapping, which helps the separation of the electrons and holes from each other [18]. Ce^{3+} ions are due to the multi-electron energy levels and variable valence states of particular interest. In addition, Ce_2O_3 is a p-type, wide band-gap semi-conducting photocatalyst [19], which may have the possibility of inducing some synergistic effects with TiO_2 (n-type semiconductor), such as a heterojunction and semiconductor-sensitized effect [20]. Ce^{+3} coupling inhibits the recombination rate of charge carriers and increases the lifetime of the charge carriers for taking part in photocatalysis [21, 22]. Yan *et al.* have suggested that coupling TiO_2 with Ce cations could reduce its bandgap due to the mixing of *4f* energy levels of the dopant with the bandgap of TiO_2, making the *4f* electron transitions allowed for the visible light activity of TiO_2 [23]. This could remarkably improve the photocatalytic activity of TiO_2. Furthermore, Zhang and Liu have reported that TiO_2 nanoparticles with Ce could effectively prohibit the recombination of the photo-generated electron-hole pairs [24]. Xu *et al.* have recently prepared a series of rare earth metal ions withTiO_2 via the sol-gel method [25]. Their results showed that incorporating TiO_2 nanoparticles with different metal ions gives rise to a red shift toward a longer wavelength in the nanoparticle absorption spectra along with an increase in interfacial electron transfer rates reducing the electron-hole pair recombination rate [26]. Also, it is revealed that metal ions could improve the thermal stability as well as the mesoscopic ordering of the mesoporous structures of the nanoparticles because they could restrain the crystallization of the titania matrix [27, 28].

Porous hexagonal boron nitride (*h*-BN) nanosheets are a type of catalyst carrier well-known for their high specific surface area, abundant pore structure, and excellent chemical and temperature stability [29]. In addition, as-synthesized *h*-BN nanostructures are intrinsically negatively charged, which allows them to be used as good h^+ carrier acceptors [30]. Hence, these materials can be employed to improve the h^+/e^- carrier separation in the photocatalyst [8, 31]. Fu *et al.* have investigated the role of *h*-BN nanoparticles on the photocatalytic activity of TiO_2. Their results showed that BN nanomaterials could improve the migration of h^+ from TiO_2 to their surface *via* electrostatic interactions and the photocatalytic activity of TiO_2 accordingly. In fact, the presence of BN sheets improves the separation of the photo-induced electron-hole pairs in TiO_2, increases the bandgap energy, and the specific surface area compared to that of pure TiO_2 nanofibers [32].

Another approach to reducing charge carriers recombination is the addition of suitable sacrificial reagents to the reaction solution. Sacrificial agents are electron donors or hole acceptors whose role in the photocatalytic generation of H_2 is critical. These compounds are easier to oxidize and reduce than water. Therefore, when they are added to the reduction solution, they can surpass water in reacting irreversibly with the photogenerated e^- or h^+. Widely used sacrificial agents are methanol, ethanol, lactic acid, and formaldehyde [33, 34]. Methanol is a good source of high-purity hydrogen [35] since it has a low boiling point and a high H/C ratio [35]. Typically, methanol acts as an effective hole-scavenger in a water-methanol mixture, resulting in greater efficiency than other organic compounds [36].

Based on the above progress, an attempt can be made to synthesize a broad-band visible-light-response TiO_2 photocatalyst modified with a rare-earth compound for efficient photocatalytic H_2 evolution from water splitting. Herein, we synthesized $BN/Ce_2O_3/TiO_2$ composite nanofibers with broad-band visible-light-response by the electrospinning technique. Unlike the previous literature reports concerning cerium + at the +II oxidation state, cerium has an oxidation state +III in our NFs. The photocatalytic activity of NFs for H_2 evolution was investigated under visible-light irradiation ($\lambda > 400$ nm) in the presence of a sacrificial agent (CH_3OH). $BN/Ce_2O_3/TiO_2$ exhibits a high photocatalytic performance (850 μmol g^{-1} h^{-1}), which is 46 and 26 times greater than the pristine TiO_2 and *h*-BN/TiO_2 nanoparticles, respectively. To complement our embedding procedure, density functional theory (DFT) within periodic boundary conditions is used to calculate the electronic density of states (DOS) of each material and to construct a complete band alignment scheme for the $BN/Ce_2O_3/TiO_2$ system. The scheme developed here should provide a solid foundation for future studies and optimization of titanium dioxide and boron nitride-based materials and devices but relevant to a wider range of metal oxide applications.

2. Experimental section

2.1. Materials

Cerium nitrate hexahydrate ($Ce(NO_3)_3.6H_2O$, 99.99%), titanium tetraisopropoxide (TTIP) ($Ti(OCH(CH_3)_2)_4$) (97%), polyvinylpyrrolidone (PVP; M_w=1300000 g/mol), acetic acid (98%), absolute ethanol (99%), absolute methanol (99%), N,N-dimethylformamide (DMF;

99.8%) and gelatine from porcine skin were purchased from Sigma Aldrich. All chemicals were used as received without further purification.

2.2. Preparation of Ce_2O_3/TiO_2 composite nanofibers

x at.% Ce:TiO_2 nanofibers (x referring to the atomic percentage of Ce in TiO_2), 1% Ce/TiO_2 (CET1), 2% Ce/TiO_2 (CET2), 3% Ce/TiO_2 (CET3), were prepared by the electrospinning method. The solution was prepared as follows. 0.3 g of PVP were added to a suspension of TTIP in ethanol (3 mL) under continuous stirring for 30 min at room temperature (precursor solution). In another beaker, a certain amount of $Ce(NO_3)_3.6H_2O$ with different mole ratios corresponding to TTIP were dissolved in ethanol (2 mL) and dimethylformamide (0.5 mL) by 30 min of stirring. Then the cerium solution and precursor solution were mixed together under vigorous stirring for 1 h. The obtained homogeneous solution was transferred to a syringe with a stainless-steel needle (diameter of 0.7 mm) at a constant flow rate of 1 mL/h. The temperature inside the chamber of electrospinning was (38 ± 5) °C. A high voltage power source (1.25 kV for each centimeter between the needle and the collector) was used in the electrospinning process. Nanofibers were collected on a rotating coil covered with aluminum foil with a rotation speed of 400 rpm. The composite nanofibers were collected and then calcined in a furnace with a heating rate of 5 °C/min at 400 °C for 4 h in air.

2.3. Exfoliation of BN

Boron nitride sheets were exfoliated from boron nitride powder with gelatin from porcine skin [37, 38]. 20 g of porcine skin gelatin were added to 80 mL of hot water (70 °C). After that 1 g of BN was added to the gelatin solution. The mixture was kept overnight in an ultrasonic homogenizer at 50 °C. Exfoliated BN was collected by centrifugation at 6000 rpm for 30 min, and the supernatant was decanted away. The resultant precipitates (exfoliated BN) were dried at 80 °C for 48 h and then calcined at 600 °C for 2 h in air with a heating rate of 5 °C/min to obtain the pure exfoliated BN.

2.4. Preparation of BN/TiO_2 (BT) and BN/2% Ce/TiO_2 (BCET) composite nanofibers

BN/TiO_2 and BN/2% Ce/TiO_2 composite nanofibers were prepared by the electrospinning process according to the methods reported in the literature [8]. The spun solution was prepared as follows. Firstly, 1.45 g (4.9 mmol) TTIP were dissolved in a mixture of ethanol (3 mL), acetic acid (2 mL) and 0.3 g of PVP and stirred for 30 min at room temperature.

Then, this solution was added to a cerium solution (0.1 mmol) in ethanol (2 mL) and DMF (0.5 mL) (precursor solution). Further, a sonicated solution of 40 mg BN in ethanol was added to the precursor solution. Next, the solution was magnetically stirred at room temperature for 1 h. Subsequently, the mixture was transferred to a syringe with a stainless-steel needle (diameter of 0.7 mm) at a constant flow rate of 1 mL/h. The temperature inside the chamber of electrospinning was 38 ± 5 °C. A high electric field strength (1.25 kV/cm) was used in the electrospinning process. Nanofibers were collected on a rotating coil covered with aluminum foil with a rotation speed of 400 rpm. The composite nanofibers were collected and then calcined in a furnace at 400 °C with a heating rate of 5 °C/min for 4 h in air.

2.5. Characterizations of nanofibers

The crystallinity and crystal structure of the nanofibers were studied using a PANAlytical Xpert-PRO diffractometer equipped with an X'celerator detector using Ni-filtered Cu-radiation (CuKα1 radiation wavelength: 0.1540598 nm, and CuKα2 radiation wavelength: 0.1544426 nm) at 40 kV and 40 mA. To obtain good quality XRD patterns, NFs were finely ground, and the obtained powder samples were scanned at a scanning rate of 0.1° min^{-1} (i.e., step size and time are 0.02° and 12 s, respectively) in the 2 h range of 10–90°. Rietveld refinement was performed using the FULLPROF program [39] with profile function 7 (Thompson-Cox-Hastings pseudo-Voigt convoluted with an axial divergence asymmetry function) [40]. The instrument resolution function was obtained from the structure refinement of a silicon standard. The morphology and structure of all nanofibers were elucidated through scanning electron microscopy (SEM, Hitachi S4800, Japan) and transmission electron microscopy TEM) on JEOL JEM 2100 (JEOL, Japan) at an accelerating voltage of 200 kV. Elemental compositions were investigated by Energy-dispersive X-ray spectroscopy (EDX) and elemental mapping using a Zeiss EVO HD15 microscope coupled with an Oxford X-MaxN EDX detector. Raman spectra were obtained using the dispersive Raman spectroscopy (Model Sentera, Bruker, Germany) using 532 nm laser [doubled Nd:YAG laser (neodymium-doped yttrium aluminum garnet)] and a power of 60 mW. FT-IR spectra were recorded in KBr disks with a Nicolet 370 FTIR spectrometer. Surface area was obtained by using N2 adsorption/desorption at 77 K (Micromeritics ASAP, France). The band gab of nanofibers was measured by a UV–Vis spectrophotometer (Jasco model V-570) equipped with a diffuse reflectance (DR) attachment (Shimadzu IRS-2200). Photoluminescence (PL) spectra were recorded via an optical fiber spectrometer (Ocean Optics usb2000). Room-temperature continuous-wave (cw) Electron Paramagnetic Resonance (EPR) measurements at X-band frequencies (9.862 GHz) were conducted with a Bruker B-ER420 spectrometer upgraded with a Bruker ECS 041XG microwave bridge and a lock-in amplifier (Bruker ER023M) using a Bruker SHQ resonator applying a modulation amplitude of 2 G and a modulation frequency of 100 kHz. The samples were measured in quartz tubes of 2.9 mm outer diameter. All EPR spectra are normalized to the sample mass. The elemental composition of the prepared samples was investigated by X-ray photoelectron spectroscopy (XPS) on an Escalab 250 (Thermo Fisher Scientific, USA) using a monochromatic Al K Alpha (1486.6 eV) at 2 kV and 1 μA. 400 μm of the surface diameter was analyzed during an acquisition time of 1203.5 s.

2.6. Electrochemical measurements

Generation, migration, and recombination of electrons/holes were evaluated by photocurrent response and electrochemical impedance spectroscopy (EIS) via Modu Lap XM potentiostat (Solartron Analytical, USA). For this purpose, an aqueous solution of Na_2SO_4 (0.5 M) was employed as the electrolyte with a three-electrode cell with a Pt wire as the counter electrode, Ag/AgCl as the reference electrode, and $BN/Ce_2O_3/TiO_2$ coated on indium–tin–oxide (ITO) as the working electrode. A 500 W linear halogen lamp in the range of λ = 420-600 nm served as the light source with a frequency range of 10^{-2} to 105 Hz. The working electrode was prepared by depositing a suspension of as-synthesized nanocomposites (40 µL) onto the surface of a prepared indium tin oxide (ITO) glass electrode substrate (10 × 10 mm) and dried at room temperature. The suspension was prepared by ultrasonic dispersion of 5 mg of the obtained photocatalyst in 80 μL DI, 20 μL ethanol and 40 μL Nafion followed by ultrasonication for 60 min. The EIS data were analyzed and fitted to the proposed equivalent circuit by EC-Lab software. The photocurrent *vs.* irradiation time curve was recorded at 0.0 V/SCE to 1.1 V/SCE under dark (20 s) and light (20 s), respectively, at a scan rate of 10 $mV\cdot s^{-1}$. The electrochemical impedance spectroscopy (EIS) was measured on an electrochemical analyzer, and the standard three-electrode system was similar to the electrode system used for photocurrent response curves.

2.7. Photocatalytic hydrogen evaluation

Photocatalytic hydrogen generation reaction was carried out in an air-tight quartz reactor. The reaction temperature was controlled at 25 °C by a cold-water circulation system. A visible light source was employed using a 500 W linear halogen lamp in the range of 420–600 nm [41],[42]. The distance between the lamp and the aqueous solution was maintained at 10 cm.

Briefly, 50 mg of nanofibers were dispersed in 20 mL of 20% aqueous methanol solution (methanol as scavenger) and transferred to a quartz reactor. The reaction medium was purged prior to the measurement with nitrogen for 30 min for oxygen removal. Each hour, one gas sample was collected to evaluate the hydrogen amount by gas chromatography (GC-1690, Jiedao, TCD, Ar carrier) with a 5 Å molecular sieve column (3 m × 2 mm).

2.8. Computational methods

The density of states (DOS) of BCET2 was determined using plane-wave DFT, treating electron exchange and correlation with the screened hybrid HSE06 functional [43, 44], which describes well the periodic solid and indeed is known to reproduce the band gaps of all content accurately in BCET2 using tetrahedra method. The plane-wave DFT calculations were performed using the Quantum espresso code [45] with the projector augmented wave approach (PAW) [46] used to describe the interaction between the core (Ti:[Ar], O:[He]) and valence electrons. The plane-wave cutoff was 60 Ry. We used a 16 × 16 × 16 for TiO_2 and Ce_2O_3 phases and 12 × 12 × 1 for h-BN-ML with special k-points mesh centered at the Γ point. For Ce_2O_3, a number of states could be found for the hybrid functional, each corresponding to different "ligand field" configurations for the unpaired electron in the Ce 4*f* orbitals These settings provided a total energy convergence within 10^{-6} eV/atom [47]. The band gap calculations were performed using unit cells derived from the experimental lattice parameters, with the ions kept at their experimentally determined positions

3. Results and discussion

To synthesize a broad-band visible-light-response TiO_2 photocatalyst, TiO_2 was modified with a rare-earth compound (Ce_2O_3) for efficient photocatalytic H_2 evolution from water splitting. Furthermore, the role of *h*-BN nanoparticles on the photocatalytic activity of TiO_2 was investigated. Effect of crystallinity of TiO_2, loading TiO_2 with cations, coupling TiO_2 with other semiconductors, and adding sacrificial reagents to the reaction solution, on photocatalytic activity of TiO_2 has been studied.

3.1. The structural and morphological properties of CETx and BCET2 NFs

To better understand the crystal structure and phase compositions of the synthesized nanofibers, the X-ray diffraction (XRD) patterns of the samples were recorded, as shown in Fig. 1. The characteristic reflections of anatase TiO_2 (JCPDS No. 01-084-1285) can be observed in the XRD patterns of all nanofibers. The XRD reflections of anatase TiO_2

appearing at 2θ = 25.3º, 37.8º, 47.9º, 53.9º, 55.1º and 62.6º, can be well indexed to the (101), (004), (200), (105), (211) and (204) diffraction planes of anatase TiO_2, respectively [48]. As shown in Table 1, Rietveld refinement of XRD data reveals that introducing small concentrations of Ce^{3+} (1-<3.0 at%) into the electrospinning solution leads to (i) the formation of small amounts of rutile and brookite phases, (ii) a decrease in the crystallite size of the main anatase phase and (iii) a slight decrease in the *c* parameter and unit cell volume of the anatase phase. In contrast, only the anatase phase, which has a similar crystallite size and lattice parameters to that formed in the undoped sample, is observed when 3 at.% Ce is used. These results suggest that Ce^{3+} ions did not substitute Ti^{4+} ions in the lattice of both anatase and rutile phases, which can be explained by the large difference in the ionic radius of Ti^{4+} and Ce^{3+} ((r (Ti^{4+}) = 60.5 pm, r (Ce^{3+}) = 101.7 pm, all cations are 6-fold coordinated) [49]. Thus, the substitution of smaller Ti^{4+} by larger Ce^{3+} cations should be accompanied by an increase in the lattice parameter and unit cell volume of the TiO_2 lattice. In contrast, a slight decrease in the *c* parameter and unit cell volume of anatase TiO_2 is observed with increasing the amount of Ce. This decrease can be explained by the decrease in the crystallite size of the anatase TiO_2 phase. These results are in good agreement with previous studies on nanocrystalline Ce coupled with TiO_2 [50], which showed that the large Ce^{3+} ions could not enter the TiO_2 lattice, but they may substitute Ti^{4+} ions on the surface of the TiO_2 crystallites. As a result, Ce-O-Ti bonds are formed on the surface of TiO_2 crystallites, which would hinder the growth of the anatase phase by reducing the interactions between crystallites and the rearrangement of Ti and O atoms in the lattice, leading to a decrease in crystallite size of the Ce incorporated TiO_2. However, this effect is not observed at a higher amount of Ce (i.e., 3 at%), which might be due to the aggregation of Ce salts during the electrospinning to form amorphous or nanocrystalline Ce_2O_3 on the surface of TiO_2 nanofibers. Thus, the anatase phase in the BN/3% Ce/TiO_2, CET3, sample shows similar structural properties to that in the unmodified TiO_2 sample. Similarly, the addition of BN to the electrospinning solution leads to a decrease in the crystallite size of the anatase phase and the formation of small amounts of brookite phases. The slight decrease in the *c* parameter and unit cell volume of the anatase phase with BN additions can also be explained by the reduction of its crystallite size [50, 51]. Rietveld refinement showed the presence of crystalline *h*-BN in BCET2 sample around 7.2 wt.%. In contrast, the amount of *h*-BN in the BT sample, is found to be 16.5 wt.%, which is higher than determined in BCET2 sample. This result suggests the presence of a small amount of amorphous BN in the BCET2 sample, as further confirmed by EDX analysis in Table S1.

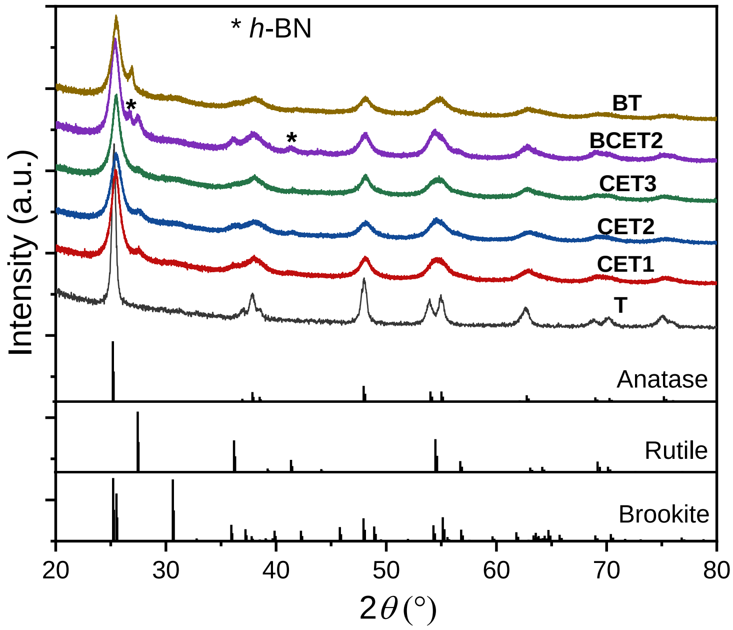

Fig. 1: XRD pattern of T, CET1, CET2, CET3, BT and BCET2 samples. The calculated XRD patterns corresponding to the anatase, rutile and brookite structures of TiO_2 are shown at the bottom. Star (*) symbols refer to the XRD reflections of *h*-BN phase.

Table 1 A summary of structural parameters extracted from XRD patterns by Rietveld refinement of T, CET1, CET2, CET3, BT, and BCET2 samples showing weight fraction wt. [%], lattice parameters a, b, c [Å], the unit cell volume V [Å^3], and crystallite size [nm].

Sample	**Weight fractions (wt%)**				**Crystallite size (nm)**				**Lattice parameters**	
	A-TiO_2	**R-TiO_2**	**B-TiO_2**	**BN**	**A-TiO_2**	**R-TiO_2**	**B-TiO_2**	**BN**	**A-TiO_2**	**R-TiO_2**
T	100	-	-	-	15.9(9)	-	-	-	a =3.7891(3) c=9.5026(9) V=136.43(1)	-
CET1	80.5(3)	10.2(2)	9.3(2)	-	6.1(4)	7.0(4)	3.7(2)	-	a =3.7771(2) c=9.4539(5) V=134.88(1)	a =4.5866(4) c=2.9409(4) V=61.87(1)
CET2	78.2(3)	12.4(2)	9.4(2)	-	5.0(3)	7.1(4)	3.8(2)	-	a =3.7743(2) c=9.4421(6) V=134.51(1)	a =4.5843(3) c=2.9428(3) V=61.85(1)
CET3	82.2(3)	7.4(2)	10.4(3)	-	6.1(4)	7.4(4)	4.1(2)	-	a =3.7765(1) c=9.4585(4) V=134.90(1)	a =4.5893(7) c=2.9335(6) V=61.79(1)
BT	74.2(4)	-	9.3(2)	16.5(3)	5.6(3)	-	4.2(2)	16.1(9)	a =3.7778(1) c=9.4514(3) V=134.89(1)	-
BCET2	71.3(3)	14.2(2)	7.3(2)	7.2(2)	6.3(4)	9.1(5)	4.3(2)	21.0(9)	a =3.7826(1) c=9.4715(3) V=135.52(1)	a =4.5885(2) c=2.9515(2) V=62.14(1)

Furthermore, the effect of BN and Ce_2O_3 on the crystal structure of TiO_2 nanofibers was studied by Raman spectroscopy. As shown in Fig. 2a and 2b, the Raman spectra of the T sample exhibited Raman-active modes of TiO_2 anatase phase at 146.9 cm^{-1} (E_g), 202.9 cm^{-1} (E_g), 396.8 cm^{-1} (B_{1g}), 513.7 cm^{-1} (A_{1g}, B_{1g}) and 635.6 cm^{-1} (E_g) [52]. In contrast, the addition of Ce_2O_3 to the nanofibers results in the formation of a rutile structure, as identified by its Raman bands at 429.5 cm^{-1} and 608.1 cm^{-1} [52]. Moreover, the Raman bands detected at 127.7 cm^{-1} and 251.1 cm^{-1} in spectra of all samples, except the T sample, can be assigned to the brookite structure [8, 52, 53], which is consistent with the XRD analysis. Moreover, the presence of a *h*-BN phase in the BT and BCET2 samples is confirmed by its characteristic E_{2g} mode located at 1359.9 cm^{-1} [8].

The structural characteristics of the synthesized nanofibers were further investigated by FTIR spectroscopy. As shown in Fig S1, all samples possess absorption bands at 650-900 cm^{-1}, which can be assigned to the Ti–O vibration [37, 54]. Besides, the absorption bands observed at 2800-2900 cm^{-1} can arise from C-H stretching vibrations of the organic part. Moreover, the BN-containing nanofibers show additional absorption bands at 800 cm^{-1} and 1381 cm^{-1}, which can be attributed to the out-of-plane bending of sp^2-bonded B–N–B and the in-plane stretching of sp^2-bonded B–N, respectively [55]. Additional peaks at 1238 cm^{-1} and 894 cm^{-1} attributed to B–O in-plane and out-of-plane bending, respectively, prove that *h*-BN nanosheets are partially oxidized on the surface [56].

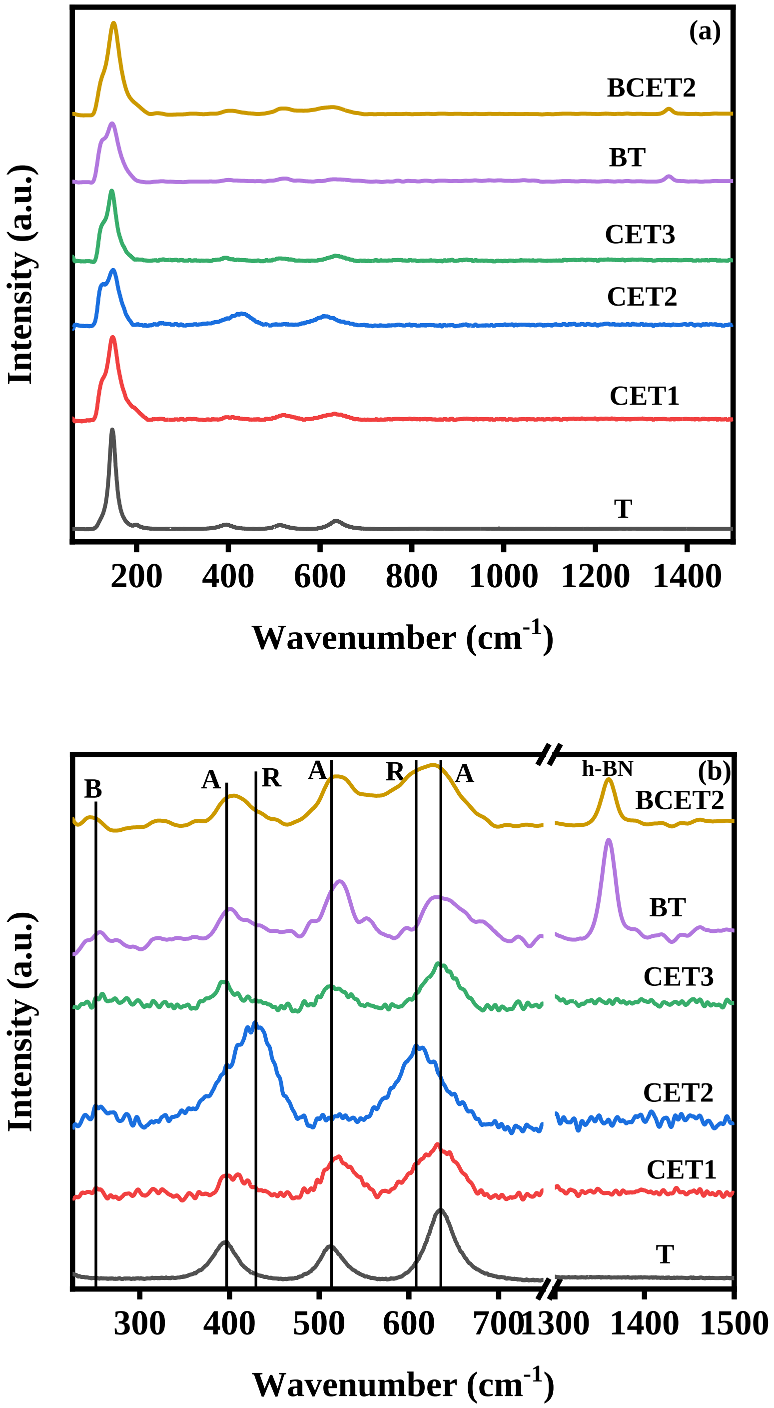

Fig. 2 (a&b) Raman spectra of T, CET1, CET2, CET3, BT and BCET2 with characteristic vibrational bands of brookite (B), anatase (A), rutile (R) and phases.

The morphology and structure of the synthesized photocatalysts were explored using SEM (Fig. 3 a-f) and TEM (Fig 3 g-h and Fig. S2). As shown in Fig. 3 a-f, SEM images reveal that CETx and BCET have a highly interconnected network morphology composed of continuous but randomly oriented nanofibers. Moreover, the diameter of the obtained nanofibers decreases from 240 nm for pristine TiO_2 to 101 nm, 70 nm, 40 nm for CET2, BT and BCET2, respectively, as shown in Fig. S2. The decrease in the diameter of TiO_2 nanofibers with Ce incorporation can be explained by the large difference in the ionic radius of Ti^{4+} and Ce^{3+} ((r (Ti^{4+}) = 60.5 pm, r (Ce^{3+}) = 101.7 pm, all cations being 6-fold coordinated) [49]. Thus, Ce cations cannot be incorporated in the TiO_2 lattice, causing a perturbation in the anatase crystal structure and blocking the crystal growth [57]. In order to confirm the influence of cerium incorporation on the structure of TiO_2 phases, the nanofibers were further analyzed by HRTEM (Fig. 3 g and h). The tetragonal structure of TiO_2 in the samples T and BCET2 was confirmed with the measured interplanar spacing of (0.35 ± 0.01) nm and (0.32 ± 0.01) nm, respectively, corresponding to the (101) plane (Fig. 3 g and h, inset). The shrinking of d-spacing of BCET2 in comparison to TiO_2 could be related to the effect of BN and Ce_2O_3 on TiO_2 lattice. In addition, The measured interplanar spacing 0.58 nm corresponding to the (011) plane of Ce_2O_3, have been detected in BCET2 nanofibers [58, 59]. The SAED pattern of TiO_2 and BCET2 are displayed in the inset of Fig. (1 h and i), showing that the crystallinity changes from pure anatase to a multi-phase mixture by the incorporation of cerium. In addition, there is a good dispersion of BN and Ce_2O_3 in TiO_2 nanofibers as confirmed by the EDX-mapping (Fig. S3) [60].

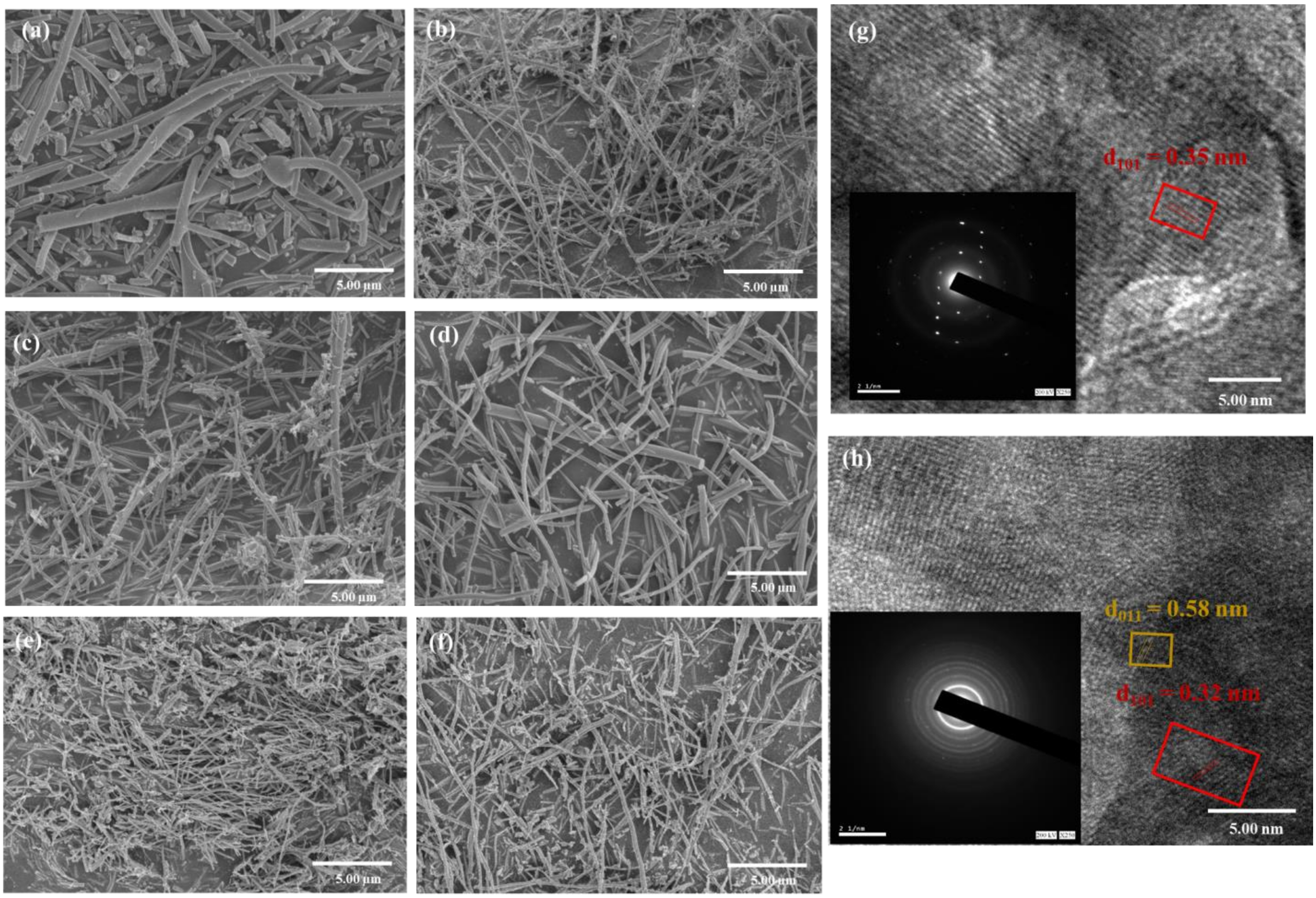

Fig. 3 Scanning electron microscope images of a) T, b) CET1, c) CET2, d) CET3, e) BT, f) BCET2, and high-resolution transition microscope of T (g) and BCET2 (h) as well as the SAED pattern of T in inset (g) and BCET2 in inset (h).

When the size of the crystallite decreases, the surface area is expected to increase. In consistent with XRD and TEM results, BET results showed that surface area of T, CET1, CET2, CET3, BT, and BCET2 nanofibers are 9, 32, 51, 49, 13, and 65 m^2 g^{-1}, respectively, which suggests a decrease in the size of the crystallite and/or the nanofibers with increasing the amount of Ce. It worth noting that the enhancement of surface area is a key factor to improve photocatalytic activity. Larger specific surface area of BCET2 could allow rapid diffusion of reactants and products and thus enhancing the photocatalytic reaction [8].

Additional information on the effect of the presence Ce_2O_3 in TiO_2 on the chemical composition of the prepared nanofibers was obtained by using X-ray photoelectron spectroscopy (XPS). The high-resolution XPS spectra of O 1s, Ti 2p, Ce 3d, and N 1s orbitals are displayed in Fig. 4 a–d. As presented in Fig. 4a, the O 1s spectrum can be fitted with three peaks at ~529.7 eV, 531.5 eV, and 532.9 eV corresponding to the oxygen atoms of the lattice, the surface adsorbed oxygen atoms, and the oxygen atoms of adsorbed water, respectively [8]. There is a slight shift to higher binding energy of ~0.02 eV compared to the T sample due to the presence of Ce_2O_3 in TiO_2 [61]. Moreover, in Fig. 4b, the Ti 2p spectrum can be fitted with a doublet peak corresponding to Ti^{4+} in the TiO_2 matrix at about 458.6 eV and 464.3 eV, which are attributed to the Ti $2p_{1/2}$ and Ti $2p_{3/2}$, respectively [8]. These characteristic peaks of Ti 2p are shifted to lower binding energies by about ~0.2 eV in the presence of Ce_2O_3 in the nanofibers due to charge transfer from Ce^{3+} to Ti^{4+} through Ce-O-Ti as the Pauling electronegativity value of Ce(1.12) is lower than that of Ti (1.5). These confirmed the interactions between Ce and TiO_2 nanofibers. In addition, this shift might also be due to the partial reduction of Ti^{4+} [31]. As shown in Fig. 4 c, the Ce 3d spectrum presents doublet peak corresponding to Ce $3d_{5/2}$ and Ce $3d_{3/2}$ spin-orbit at 881.4 eV and 899.8 eV, respectively, with ΔE (Ce 3d)= 18.4 eV [62, 63]. The strong satellite peaks located at around 885.5 eV and 903.8 eV are attributed to the Ce^{3+} ($3d^{10}$ $4f^1$) of Ce_2O_3 [64]. The N 1s peak at 398.04 eV in the XPS spectra of BT and BCET (Fig.4d) confirms the presence of *h*-BN in these two samples. The shift of the N 1s peak to lower binding energy in BCET2 compared to the BT sample by 0.02 eV proves the engagement of BN nanosheets with Ce_2O_3 and TiO_2 nanofibers [8]. According to the reported literatures [65],[66],[67], Ce_2O_3 will be stabilized through interaction by metal (Ag) and the charge transfer can stabilize Ce_2O_3. According to our results, there is charge transfer between Ce-Ti, and this interaction has stabilized Ce in +3 oxidation state.

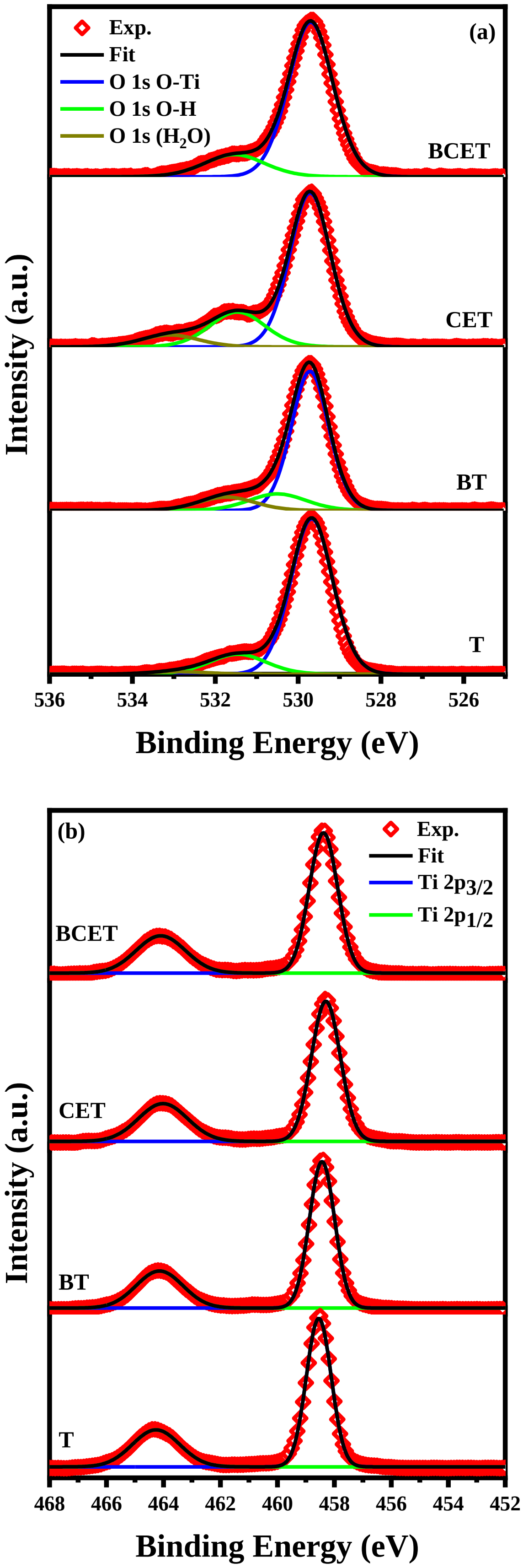
(a)
Exp.
Fit
O 1s O-Ti
O 1s O-H
O 1s (H_2O)
BCET
CET
BT
T
536
534
532
530
528
526
Binding Energy (eV)
Intensity (a.u.)
(b)
Exp.
Fit
Ti $2p_{3/2}$
Ti $2p_{1/2}$
BCET
CET
BT
T
468
466
464
462
460
458
456
454
452
Binding Energy (eV)
Intensity (a.u.)

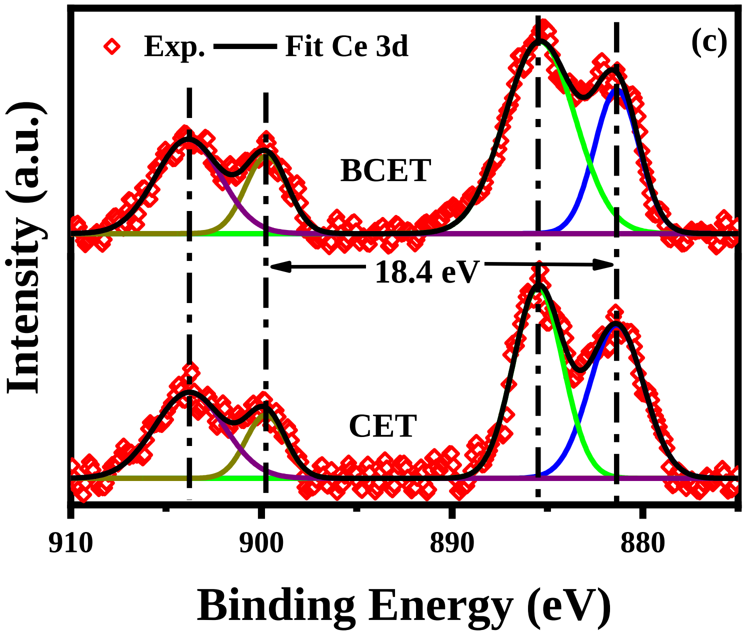

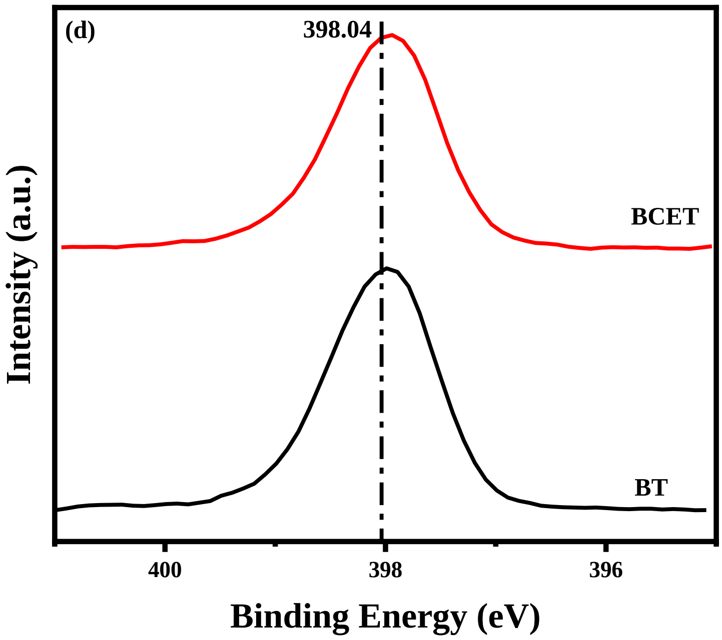

Fig. 4. High-resolution XPS spectra of O 1s (a), Ti 2p (b), Ce 3d (c) and N 1s (d) for T, BT, CET and BCET nanofibers.

The RT cw EPR measurements at X-Band frequencies show for all samples a relatively sharp, basically symmetrical line ($\Delta B_{pp} \approx 5$ G) around g = 2.002 - 2.004. Compared to the TiO_2 reference, the signal intensity strongly decreases for samples with increasing Ce content, and the signal position shifts to slightly higher g-values. Also, the addition of BN results in lower signal intensity and a signal position shifted to higher g-values with respect to the TiO_2 reference. However, the effect of BN addition to a sample with 2.0 at.% Ce only has a slight effect on the EPR signal. The signal intensity appears to be even slightly lower and the position shifts slightly larger in the absence of BN. A symmetrical EPR signal around g ≈ 2.003-2.004 has been reported for TiO_2 samples before and was attributed to a trapped electron at an oxygen vacancy which has been suggested by some authors to be located at the surface, while others assigned it to bulk defects (see, e.g. [68] and references therein). While the location of the oxygen vacancy cannot be clearly determined from these measurements, a location at the surface is consistent with the interpretation of XRD and SEM results, suggesting rather a surface than a bulk modification.

In fact, Ce was selected as a coupling element in our study considering that the shift of Ce^{4+}/Ce^{3+} can accelerate charge separation. The impurity levels caused by Ce_2O_3 incorporation enables TiO_2 to be excited in the visible region [69]. The impurity levels formed by Ce_2O_3 incorporation and *h*-BN exfoliation, extend the wavelength response to the visible region. In addition, the conversion between the two valence states of Ce^{3+} and Ce^{4+} can separate the electron–hole pairs and promote the reaction. The stabilization of anatase phase is happening by the surrounding cerium ions through the formation of Ce–O–Ti bonds at the interface. Titanium ions substitute for the cerium ions in the lattice of cerium oxide to form octahedral Ti sites [69]. Ce^{3+} resides in the octahedral interstitial site for TiO_2 with the high oxygen affinities, where it creates localized positive charge around titanium or forms an oxygen vacancy [70]. The amount of oxygen vacancies formed for compensating the charge difference between Ti^{4+} and Ce^{3+} are expected to be increased with increasing the amount of Ce^{+3} incorporating in the TiO_2 lattice.

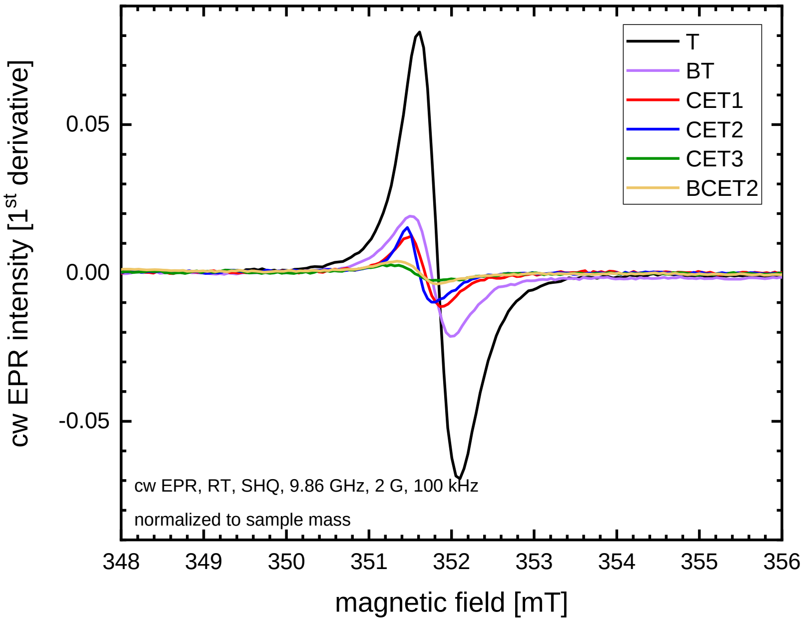

Fig. **5** cw EPR measurement at room temperature of T, BT , CET1, CET2, CET3, BCET2.

The reflectance spectra of prepared nanofibers are shown in Figure 6. The band gap of the nanostructures was graphically calculated from Figure 7 according to the Kubelka-Munk equations (1) and (2) [71]:

$$F = ((1-R)^2)/2R \qquad \textbf{(1)}$$

$$(Fh\nu)^{1/2} = A(h\nu - Eg) \qquad \textbf{(2)}$$

where F, R, hν and Eg represent the Kubelka–Munk function, reflectance, photon energy and band gap, respectively. The obtained values were 3.12 ± 0.03, 3.12 ± 0.04, 3.06 ± 0.01, 3.03 ± 0.03, 2.96 ± 0.04 eV and 2.82 ± 0.07 eV for T, BT, CET1, CET2 and CET3, BCET2 respectively. In the TiO_2 sample (T), the absorption in the ultraviolet range is associated with the charge transfer transition from O 2p to Ti 3d electronic orbitals [72]. The introduction of Ce atoms into the TiO_2 lattice could be complicated due to the mismatch of ion radii of Ce^{4+}/Ce^{3+} and Ti^{4+} [73]. It is assumed that Ce can form CeO_2/Ce_2O_3 on the surface of TiO_2 nanofibers [73]. Transitions between Ce^{4+} and Ce^{3+} can occur due to redox reactions [37, 73-77]. It was shown that forming of CeO_2/TiO_2 heterostructure results in forming of shallow donor levels in the TiO_2 band gap [37, 73-77]. The red-shift in the absorption band could be a result of the charge-transfer transition between shallow donor sites and the valence band of the host TiO_2 [37, 73-78].

On the other hand, with the addition of Ce_2O_3 and BN to the surface of TiO_2 nanofibers, the light absorption edges of TiO_2 nanoparticles were knowingly red shifted to the visible light region, in which Ce_2O_3, *h*-BN co-incorporated TiO_2 sample exhibits the highest visible light absorption capability, proving that TiO_2 nanocomposites with Ce_2O_3 and *h*-BN species play a synergistic effect in the development of light absorption. The band gap of the BCET2 sample decreases compared with that of BT NF. Obviously, the BCET2 nanofiber significantly reduces the corresponding band gap energy, which is lower than that of the BT. BCET2 composite nanofibers had the lowest band gap values out of the series of samples.

PL spectra of the samples are shown in Figure 8. The TiO_2 PL spectrum displays a wide peak, centered at 500 nm. The TiO_2 PL emission can be explained by oxygen vacancies and self-trapped excitons [37, 77]. Formation of donor levels within the TiO_2 band gap is suppressed in Ce_2O_3/TiO_2 nanofibers, such as charge transfer to exciton and vacancy states [74]. As a result, quenching of photoluminescence in the composite nanofibers was found for the samples containing Ce, but also the addition of BN resulted in a reduced photoluminescence. In agreement with the interpretation of the photoluminescence spectra, the EPR measurements also suggest a lower content of (paramagnetic) oxygen vacancies for samples containing Ce or BN.

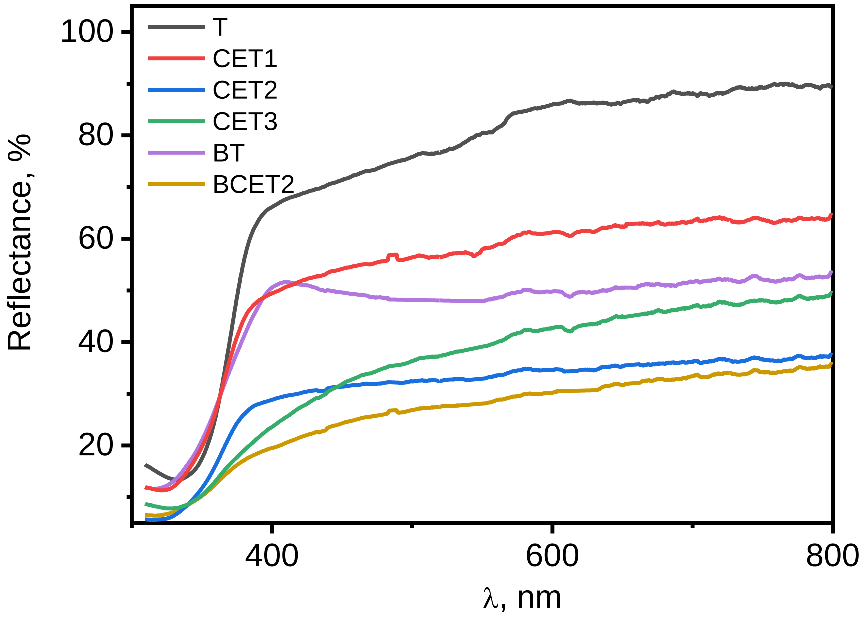

Fig. 6 Diffuse Reflectance spectra of T, CET1, CET2, CET3, BT and BCET2 nanofibers.

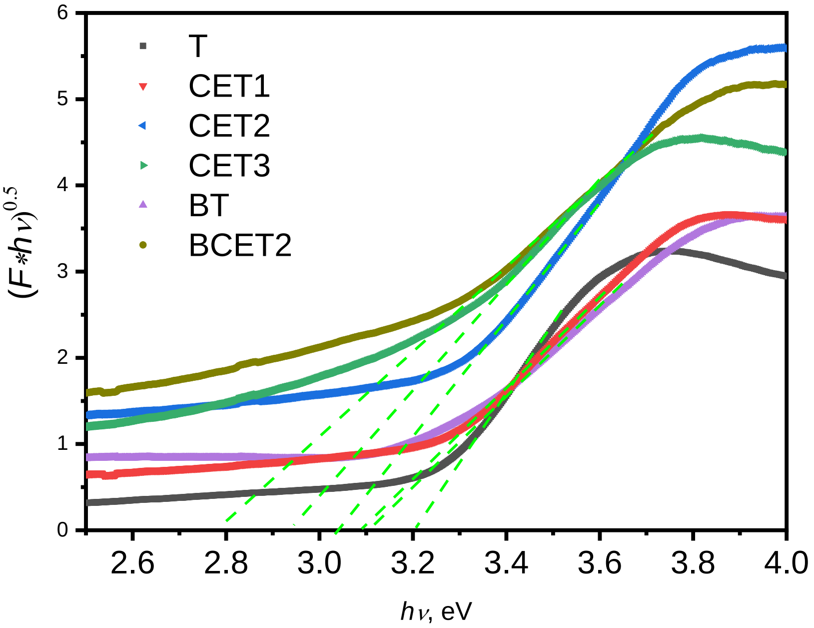

Fig. 7 Plot of Transformed Kubelka – Munk function against the energy for T, CET1, CET2, CET3, BT and BCET2 samples.

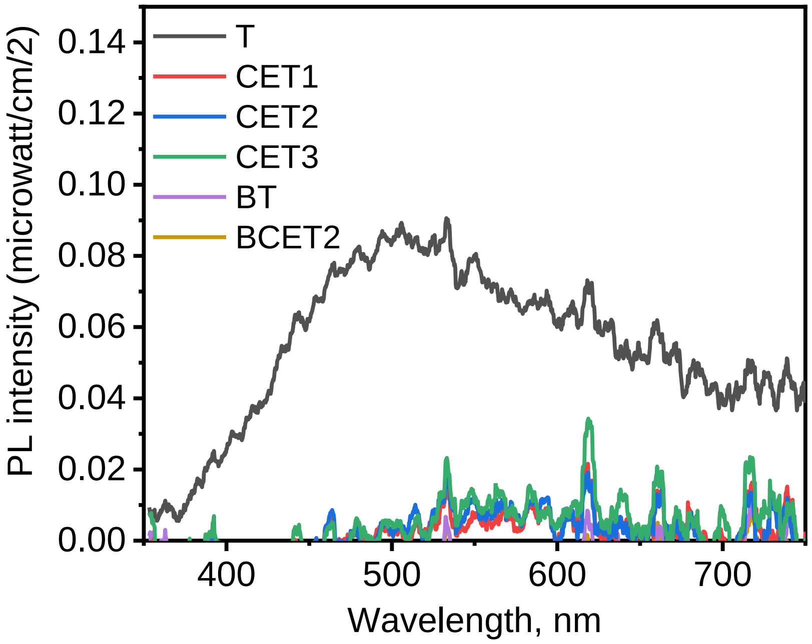

Fig. 8 Photoluminescence spectra of T, CET1, CET2, CET3, BT and BCET2 nanofibers.

3.2. Photo-electrochemistry tests

To predict the mechanism of photocatalytic hydrogen evolution performance of synthesized photocatalysts, electrochemical impedance spectroscopy (EIS) was carried out, as shown in Fig. 9. The results show that the arc radius of the Ce_2O_3/TiO_2 electrode is much smaller than that of the TiO_2 electrode. Also, the arc radius of BCET2 is smaller compared to the one for bare TiO_2 and *h*-BN (T, BT), respectively. The results, moreover, suggest that the Ce_2O_3/TiO_2 electrode has a much higher separation efficiency of photogenerated electron-hole pairs and faster charge-transfer than the TiO_2 electrode at the solid-liquid interface. Therefore, incorporating Ce_2O_3 and *h*-BN in TiO_2 is a promising way to improve its photocatalytic efficiency [79]. The resistance formed at the interface of the nanofibers and electrolyte (R_2) was 7.44, 5.27, 2.98, 3.72, 4.89 and 2.27 kΩ for T, CET1, CET2, CET3, BT and BCET2, respectively. Moreover, the addition of Ce reduces the impedance significantly, indicating a lower charge transfer resistance across the electrode/electrolyte interface. In addition, BCET2 exhibits the smallest arc radius and the lowest impedance, which can facilitate both the interfacial charge transfer process and separation efficiency of photo-induced carriers [80-82]. While both EPR and PL suggest a reduced amount of defects by the addition of Ce or BN, a more detailed analysis of the magnitude of the effect in comparison to the EIS results strongly suggests the importance of an additional mechanism for improved electronic properties.

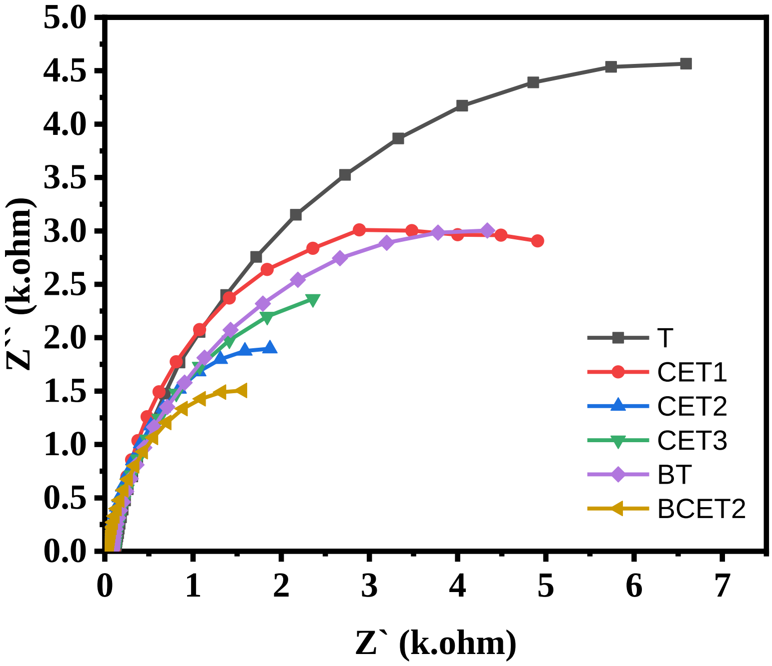

Fig. 9 EIS of TiO_2, Ce/TiO_2 with different contents of Ce and *h*-BN/TiO_2 composites.

3.3. H_2 generation reactions

The photocatalytic performance of as-synthesized compounds was investigated through the water splitting under visible light irradiation. Fig. 10 a displays the photocatalytic activity of Ce_2O_3/TiO_2 nanofibers for hydrogen evolution from the aqueous solution containing methanol as a scavenger. Methanol molecules scavenge the holes and thus decrease the recombination of electrons and holes, allowing the electrons to react with the protons to produce hydrogen. Nada *et al.* [8], Arda Yurtsever *et al.* [83], Liu *et al.* [84], and Vinothkumar *et al.* [85], have referred to the methanol role in photocatalytic reactions, as shown in Table 2.

The pure TiO_2 nanofibers show a low photocatalytic activity for H_2 production (110 $\mu mol \cdot g^{-1} \cdot h^{-1}$). This can be attributed to the rapid recombination between electrons-holes and the wide bandgap of TiO_2 (3.19 eV) [86]. However, with the presence of Ce_2O_3 on the surface of TiO_2 nanofibers, a significant enhancement in the rate of H_2 evolution is observed. The improved photocatalytic performance suggests that Ce acts as a good co-catalyst for H_2 evolution, and the heterojunction formed between Ce_2O_3 with TiO_2 plays an essential role in an efficient charge separation across the interface. Hence, the enhanced photocatalytic activity of the prepared nanocomposites is due to the synergistic effect of the heterojunction composition in both increasing the optical absorption of TiO_2 and decreasing the recombination rate between electrons and holes in the heterostructure system. Similar results have been reported by Liu *et. Al* . [84] and Yurtsever *et. al* [83], about rare earth metal oxide combined with TiO_2 photocatalytic activity, as shown in Table 2.

In order to study the dependency of the photocatalytic activity of the nanocomposites upon the Ce_2O_3 ratio, a variety of samples with different amounts of Ce_2O_3 and a constant amount of TiO_2 were prepared. As shown in Fig. 10.a, the CET2 shows the highest photocatalytic activity giving a hydrogen evolution rate of 1880 $\mu mol \cdot g^{-1} \cdot h^{-1}$. Therefore, we can conclude that there is an optimal ratio of $Ce:TiO_2$ for maximum hydrogen production. The use of lower amounts of Ce% may simply decrease the number of active catalytic sites on the nanoparticle, reducing the nanocomposite's overall photocatalytic activity. In addition, the sample with CET3 shows a lower H_2 evolution rate (1410 $\mu mol \cdot g^{-1} \cdot h^{-1}$) than the CET2, which demonstrates that a further increase in the amount of Ce causes the "shielding effect" of Ce that reduces the photocatalytic performance.

In order to investigate the role of BN and Ce in the photocatalytic activity of the prepared photocatalysts BT and BCET2, the hydrogen evolution performance of enhanced

TiO_2 nanofibers was measured (Fig. 10.a). According to the results, the H_2 evolution rate increases from 110 μmol·g^{-1}·h^{-1} to 194 μmol·g^{-1}·h^{-1}, with the presence of *h*-BN on TiO_2, and for Ce_2O_3 and *h*-BN on TiO_2, the H_2 evolution rate is further enhanced to 5100 μmol·g^{-1}·h^{-1}, which is 46 and 26 times greater than the pristine TiO_2 and *h*-BN/TiO_2 nanofibers respectively.

The significant enhancement in the H_2 evolution rate of BCET2 can likely be attributed to the co-catalyst effect of *h*-BN on the surface of the TiO_2 and its contribution to restrict the re-combination of e^-/h^+ and the enhancement of the lifetime of photo-excitons, as well as to the two-step photo-excitation mechanism provided by Ce, which affords outstanding catalytic peerformance for the hydrogen production in BCET2 [87]. The two-step photo-excitation mechanism can be explained by considering that electrons in the valence band of TiO_2 can get excited to the empty *4f* orbitals of Ce by absorbing low energy photons and move to the conduction band of TiO_2 through there, by absorbing another low energy photon. The hybridization of N_{2p} (from BN) and O_{2p} (from TiO_2) orbitals shift the valence band upward, resulting in a reduction in the TiO_2 band gap. This phenomenon lessens the photo-energy required for the electronic excitations in between the valence and conduction bands and ultimately enhances the TiO_2 performance. The photo-excitation takes place from this energy level to the TiO_2 conduction band, requiring absorbing the low energy photons. Therefore, the synergistic effect of *h*-BN and Ce allows the participation of a large number of electrons in the photocatalytic redox reactions, subsequently enhancing the activity of TiO_2 [88]. Therefore, it could be inferred that BN and Ce_2O_3 would play an important synergistic role in enhancing photocatalytic hydrogen production. In addition, other results have been published about co-incorporation with N, B, BN and graphene, as shown in Table 2 [89]. In comparison with other photocatalysts, our nanofibers have good photocatalytic activity.

The stability and recyclability of the photocatalysts were examined in four consecutive runs. Each cycle lasted for 6 h under visible light irradiation. As shown in Fig. 10 b, the H_2 production rate of BCET2 is quite the same after four runs, indicating the excellent reusability and stability of BCET2 nanofibers.

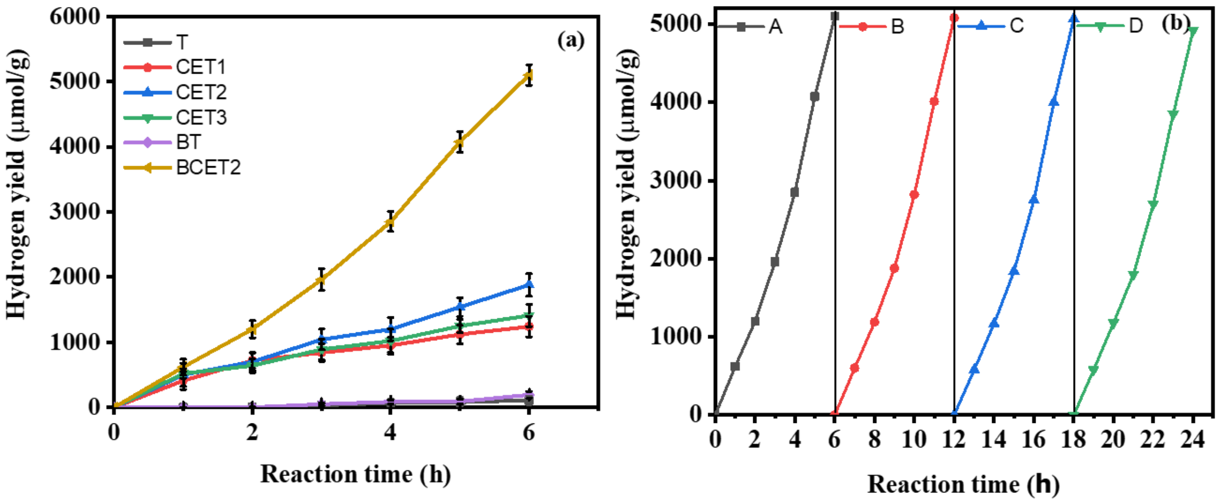

Fig. 10 a) Photocatalytic performance for H_2 evolution over prepared nanofibers. b) Recycling test for the hydrogen evolution performance of BCET2 nanofibers.

Table 2 Doped TiO_2 catalysts for photocatalytic hydrogen production.

Catalyst	Preparation technique	Output: H_2 production	Sacrificial agent	References	Light source
BCET2	Electrospinning	850 µmol g^{-1} h^{-1}	Methanol	This work	500W linear halogen lamp
CET2	Electrospinning	313 µmol g^{-1} h^{-1}	Methanol	This work	500W linear halogen lamp
0.5% Er doped TiO_2 0.1 g	Sol gel technique	45 µmol g^{-1} h^{-1}	Methanol	[83]	Osram Ultravitalux 300 W UV-VIS lamp
(Yb, Er) NYF-TiO_2/Au 500 mg	Hydrothermal method	870 µmolg^{-1} h^{-1}	Ethanol	[90]	Solar AM 1.5 with filter UV-Cut off, visible cut off, IR-cut off and under full spectrum
Au/TiO_2 500 mg	Hydrothermal method	200 µmol g^{-1} h^{-1}	ethanol	[90]	Solar AM 1.5 with filter UV-Cut off, visible cut off, IR-cut off and under full spectrum
TiO_2 -2 La-600-Pt (0.2 g) TiO_2-0La-	Sol–gel method	3500 µmol g^{-1} h^{-1} 825 µmol h^{-1}	Methanol methanol	[84]	500 W high pressure mercury lamp
0.1% Nd^{3+}-doped TiO_2	Sol–gel method	3400 µmolg^{-1}h^{-1}	methanol	[91]	300 W Xe lamp

0.5 g					
Eu-TiO_2/graphene 50 mg	Hydrothermal	100 µmolg^{-1} h^{-1}	0.1 M Na_2S and 0.04 M Na_2SO_3	[92]	metal halogen lamp (GQIBT, 400 W/D, ODRAM, Germany)
Ag/Ce-TiO_2 0.2mM Ag 0.3mM Ce	---	1.47 µmol cm^{-2}.h^{-1}	Ethanol	[93]	Visible light (Xe lamp with optical filter), UV (high pressure Hg lamp)
NY TiO_2-Pt	---	20.88 mmol g^{-1} h^{-1}		[94]	Visible light and UV (PLSSXE-300C Xe lamp)
La^{+3}/TiO_2-CdS 0.1 g	Simple mechanical mixed method	2260 µmolg^{-1}h^{-1}	0.10 M Na_2S and 0.020 M Na_2SO_3.	[95]	400W high-pressure mercury lamp
Yttrium doped TiO_2 (Y:TiO_2) nanoparticles 10 mg	Wet chemical methods	44 µmol g^{-1}h^{-1}	Ethanol	[96]	300 W Xenon Vis
Ce–N–TiO_2 0.2 g	Co-precipitation method	1030 µmolg^{-1}h^{-1}	methanol	[85]	500-W tungsten halogen lamp
La^{+3}/TiO_2: B,N 0.02 g 1.5% La	Hydrothermal method	2400 µmol g^{-1} h^{-1}	K_2CO_3	[89]	300 W Xe lamp

3.4. Electronic Properties

Utilizing the calculated lattice parameters listed in Table 1. The DOS of anatase, rutile, brookite h-BN and Ce_2O_3 with the suitable high-symmetry orientations of the irreducible Brillouin zone are illustrated in Figure 11. A 3.3, 3.01, 3.32, 3.17 and 4.67 eV calculated energy band gap for anatase, rutile, brookite, Ce_2O_3 and *h*-BN were obtained, respectively. The calculated band gaps of heterostructure closed to the experimental band gap. The band gap value acquired in this structure is comparable to those previously reported of 3.36, 3.1, 3.51, 3.2 and 4.66 eV for anatase [97], rutile [97], brookite [97], Ce_2O_3 [47] and h-BN [98].

Figure 11 demonstrates that no conduction level is present near the Fermi level on the anatase surface, indicating that no surface states exist. In contrast, the rutile and Ce_2O_3 have conduction levels that are close to the Fermi level. This sequence of the energy levels is mainly due to the redundant electronics of the anatase surface migrate to rutile and Ce_2O_3 [99, 100]. The heterostructure of BCET2 has a different junction between valance bands and conduction bands, which leads to the formation of impurity energy levels (IELs). The presence of IELs enhanced the composite to be active under visible light illumination, as observed in Fig. 6 and 7. In addition, the IELs contribute to the increased separation of electrons and holes pairs and enhance the photocatalysis process by improvement of the migration of photoexcited carriers which mached with Photoluminescence spectra (Fig. 8). Moreover, the lowest VB of h-BN as compared to the other materials in the heterostructure play important role for scavenging the holes in the BCET2 system which leads to the stability between photo-excited electrons and holes to improve the stability of the nanocomposite which lead to improve the hydrogen efficiency under visible light [8].

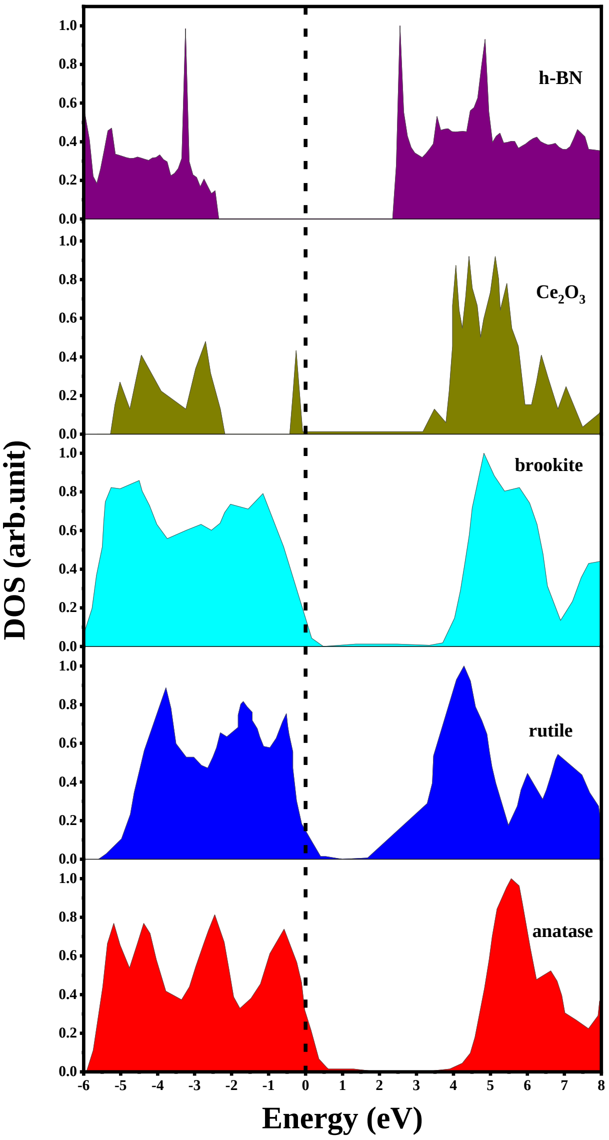

Fig. 11 Calculated density of states (DOS) for anatase, rutile, brookite, Ce_2O_3 and h-BN in BCET2 nanofibers

According to the results discussed above, the mechanism of hydrogen production using BCET2 nanofibers can be explained as follows (Fig. 12). From XRD, Raman, XPS and DOS, we can conclude that the oxygen vacancies states were above the valence band. In addition, there is different junctions (as impurity levels) formed from the valance bands and conduction bands of anatase, rutile, brookite and Ce_2O_3 as nanocomposites in the nanofiber structure. Moreover, the effect of PN heterojunction between Ce_2O_3 and TiO_2 played important role beside the impurity levels to enhance photocatalytic activity as synergistic effect inside the BCET2. When the nanofibers are excited with visible light, the electron and holes are generated. Then these electrons can reach the conduction band by absorbing the low energy photons. Hence, the conduction bands accepted more electrons under visible light. The hydrogen was produced from electrons with protons. In another hand, the holes were scavenged rapidly by *h*-BN nanosheets due to the electrostatic attraction between the positive charge of holes and the negative charge of BN [101]. In addition, the BN on the surface of the TiO_2 contributed to the enhancement of the separation of e^-/h^+ and the extension of the lifetime of photo-excitons.

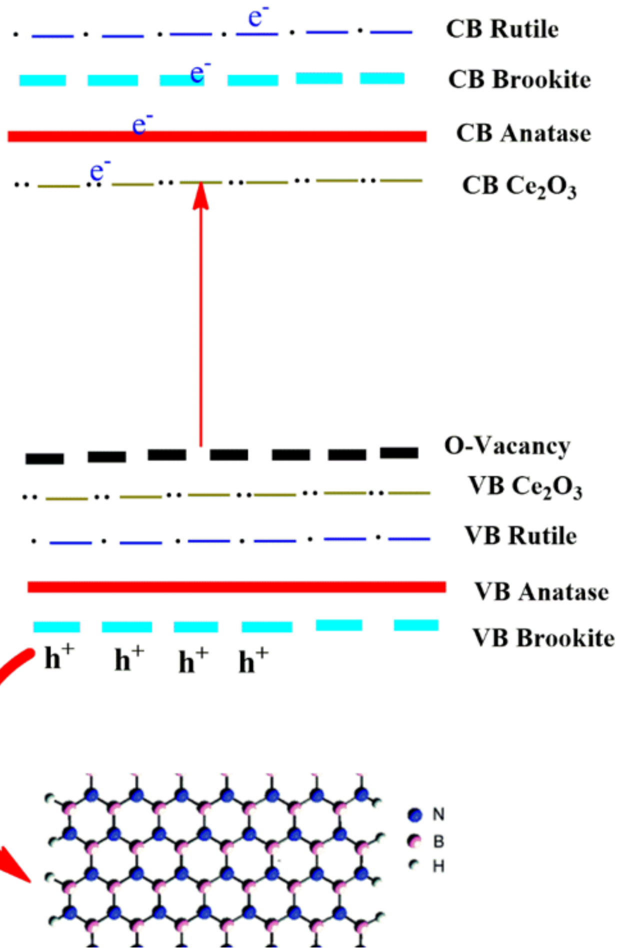

Fig. 12 Schematic representation of excitations in BCET2 under visible light

Conclusion

The current study focuses on the influence of co-incorporation of rare-earth metal (Ce) and *h*-BN into TiO_2 nanofibers on their photocatalytic properties. In summary, it can be concluded that incorporation enhances the photocatalytic properties of TiO_2 nanofibers under visible light. The enhancement of the photocatalysis depends on the cerium molar ratio and the presence of *h*-BN. This is most probably due to the existence of Ce 4f mid-gap electronic states in the BCET2. The cerium and *h*-BN showed a significant effect on the texture, structure, bandgap and particle size and also number of defects / oxygen vacancies in TiO_2. The oxygen vacancies states were above the valence band. We have experimentally demonstrated that the synergistic effect of BN exfoliation *and* cerium incorporation significantly enhances the photocatalytic activity of TiO_2. In detail, the holes were scavenged rapidly by *h*-BN nanosheets due to the electrostatic attraction between the positive charge of holes and the negative charge of BN. In addition, the BN on the surface of the TiO_2 contributed to the enhancement of the separation of e^-/h^+ and the extension of the lifetime of photo-excitons. The $BN/Ce_2O_3/TiO_2$ was examined for H_2 production in water and methanol mixtures under solar radiation. At an optimum 2 mol% Ce loading, the Ce_2O_3 and BN incorporated TiO_2 showed an exceptional activity for hydrogen production, i.e. 46 times higher than the pristine TiO_2. The reduction in the band gap and recombination between electrons/holes of BCET2 may arise due to a different junction between valance bands and conduction bands in this heterostructure, as presented in DOS. In addition, the described $BN/Ce_2O_3/TiO_2$ nanofibers can be used as a benchmark for developing hydrogen generation from photocatalysis and development as electrode for electrolysis and wastewater treatment.

REFERENCES

[1] K. Maeda, K. Teramura, D. Lu, T. Takata, N. Saito, Y. Inoue, K. Domen, Photocatalyst releasing hydrogen from water, Nature, 440 (2006) 295-295.

[2] R.D. Cortright, R. Davda, J.A. Dumesic, Hydrogen from catalytic reforming of biomass-derived hydrocarbons in liquid water, Materials For Sustainable Energy: A Collection of Peer-Reviewed Research and Review Articles from Nature Publishing Group, World Scientific2011, pp. 289-292.

[3] R.M. Navarro, M. Pena, J. Fierro, Hydrogen production reactions from carbon feedstocks: fossil fuels and biomass, Chemical reviews, 107 (2007) 3952-3991.

[4] G. Deluga, J. Salge, L. Schmidt, X. Verykios, Renewable hydrogen from ethanol by autothermal reforming, Science, 303 (2004) 993-997.

[5] X. Lang, J. Zhao, X. Chen, Visible-Light-Induced Photoredox Catalysis of Dye-Sensitized Titanium Dioxide: Selective Aerobic Oxidation of Organic Sulfides, Angewandte Chemie, 128 (2016) 4775-4778.

[6] J. Liu, Y. Liu, N. Liu, Y. Han, X. Zhang, H. Huang, Y. Lifshitz, S.-T. Lee, J. Zhong, Z. Kang, Metal-free efficient photocatalyst for stable visible water splitting via a two-electron pathway, Science, 347 (2015) 970-974.

[7] B.-S. Huang, F.-Y. Chang, M.-Y. Wey, Photocatalytic properties of redox-treated Pt/TiO2 photocatalysts for H2 production from an aqueous methanol solution, International journal of hydrogen energy, 35 (2010) 7699-7705.

[8] A.A. Nada, M.F. Bekheet, R. Viter, P. Miele, S. Roualdes, M. Bechelany, BN/GdxTi (1-x) O (4-x)/2 nanofibers for enhanced photocatalytic hydrogen production under visible light, Applied Catalysis B: Environmental, 251 (2019) 76-86.

[9] A.A. Nada, W.M. El Rouby, M.F. Bekheet, M. Antuch, M. Weber, P. Miele, R. Viter, S. Roualdes, P. Millet, M. Bechelany, Highly textured boron/nitrogen co-doped TiO2 with honeycomb structure showing enhanced visible-light photoelectrocatalytic activity, Applied Surface Science, 505 (2020) 144419.

[10] H.H. El-Maghrabi, A.A. Nada, S. Roualdes, M.F. Bekheet, Design of Ni/NiO–TiO2/rGO nanocomposites on carbon cloth conductors via PECVD for electrocatalytic water splitting, International Journal of Hydrogen Energy, 45 (2020) 32000-32011.

[11] K. Maeda, Photocatalytic water splitting using semiconductor particles: history and recent developments, Journal of Photochemistry and Photobiology C: Photochemistry Reviews, 12 (2011) 237-268.

[12] V.T. Le, H. Kim, A. Ghosh, J. Kim, J. Chang, Q.A. Vu, D.T. Pham, J.-H. Lee, S.-W. Kim, Y.H. Lee, Coaxial fiber supercapacitor using all-carbon material electrodes, ACS nano, 7 (2013) 5940-5947.

[13] A. Greiner, J.H. Wendorff, Electrospinning: a fascinating method for the preparation of ultrathin fibers, Angewandte Chemie International Edition, 46 (2007) 5670-5703.

[14] D. Astruc, F. Lu, J.R. Aranzaes, Nanoparticles as recyclable catalysts: the frontier between homogeneous and heterogeneous catalysis, Angewandte Chemie International Edition, 44 (2005) 7852-7872.

[15] L. Shao, G. Xing, L. He, J. Chen, H. Xie, X. Liang, C. Qi, Sulfonic groups functionalized preoxidated polyacrylonitrile nanofibers and its catalytic applications, Applied Catalysis A: General, 443 (2012) 133-137.

[16] L.G. Devi, S.G. Kumar, B.N. Murthy, N. Kottam, Influence of Mn2+ and Mo6+ dopants on the phase transformations of TiO2 lattice and its photo catalytic activity under solar illumination, Catalysis Communications, 10 (2009) 794-798.

[17] X. Pan, M.-Q. Yang, X. Fu, N. Zhang, Y.-J. Xu, Defective TiO 2 with oxygen vacancies: synthesis, properties and photocatalytic applications, Nanoscale, 5 (2013) 3601-3614.

[18] M. Nasir, Z. Xi, M. Xing, J. Zhang, F. Chen, B. Tian, S. Bagwasi, Study of synergistic effect of Ce- and S-codoping on the enhancement of visible-light photocatalytic activity of TiO2, The Journal of Physical Chemistry C, 117 (2013) 9520-9528.

[19] W. Cai, F. Chen, X. Shen, L. Chen, J. Zhang, Enhanced catalytic degradation of AO7 in the CeO2–H2O2 system with Fe3+ doping, Applied Catalysis B: Environmental, 101 (2010) 160-168.

[20] Y. Liu, P. Fang, Y. Cheng, Y. Gao, F. Chen, Z. Liu, Y. Dai, Study on enhanced photocatalytic performance of cerium doped TiO2-based nanosheets, Chemical engineering journal, 219 (2013) 478-485.

[21] T.-x. Liu, X.-z. Li, F.-b. Li, Enhanced photocatalytic activity of Ce3+-TiO2 hydrosols in aqueous and gaseous phases, Chemical engineering journal, 157 (2010) 475-482.

[22] B. Choudhury, B. Borah, A. Choudhury, Extending photocatalytic activity of TiO2 nanoparticles to visible region of illumination by doping of cerium, Photochemistry and photobiology, 88 (2012) 257-264.

[23] Y. Li, Q. Du, T. Liu, J. Sun, Y. Jiao, Y. Xia, L. Xia, Z. Wang, W. Zhang, K. Wang, Equilibrium, kinetic and thermodynamic studies on the adsorption of phenol onto graphene, Materials Research Bulletin, 47 (2012) 1898-1904.

[24] X. Zhang, Q. Liu, Preparation and characterization of titania photocatalyst co-doped with boron, nickel, and cerium, Materials Letters, 62 (2008) 2589-2592.

[25] Y.-h. Xu, H.-r. Chen, Z.-x. Zeng, B. Lei, Investigation on mechanism of photocatalytic activity enhancement of nanometer cerium-doped titania, Applied Surface Science, 252 (2006) 8565-8570.

[26] A.-W. Xu, Y. Gao, H.-Q. Liu, The preparation, characterization, and their photocatalytic activities of rare-earth-doped TiO2 nanoparticles, Journal of catalysis, 207 (2002) 151-157.

[27] K.L. Frindell, J. Tang, J.H. Harreld, G.D. Stucky, Enhanced mesostructural order and changes to optical and electrochemical properties induced by the addition of cerium (III) to mesoporous titania thin films, Chemistry of materials, 16 (2004) 3524-3532.

[28] K.L. Frindell, M.H. Bartl, A. Popitsch, G.D. Stucky, Sensitized Luminescence of Trivalent Europium by Three-Dimensionally Arranged Anatase Nanocrystals in Mesostructured Titania Thin Films, Angewandte Chemie, 114 (2002) 1001-1004.

[29] M. Wang, Y. Bai, B. Zhang, B. Zhong, Y. Yu, J. Zhang, X. Huang, G. Wen, Large scale fabrication of porous boron nitride microrods with tunable pore size for superior copper (II) ion adsorption, Ceramics International, 45 (2019) 6684-6692.

[30] J. Peng, S. Wang, P.-H. Zhang, L.-P. Jiang, J.-J. Shi, J.-J. Zhu, Fabrication of graphene quantum dots and hexagonal boron nitride nanocomposites for fluorescent cell imaging, Journal of biomedical nanotechnology, 9 (2013) 1679-1685.

[31] S. Kawrani, A.A. Nada, M.F. Bekheet, M. Boulos, R. Viter, S. Roualdes, P. Miele, D. Cornu, M. Bechelany, Enhancement of calcium copper titanium oxide photoelectrochemical performance using boron nitride nanosheets, Chemical Engineering Journal, 389 (2020) 124326.

[32] X. Fu, Y. Hu, Y. Yang, W. Liu, S. Chen, Ball milled h-BN: an efficient holes transfer promoter to enhance the photocatalytic performance of TiO2, Journal of hazardous materials, 244 (2013) 102-110.

[33] T. Sreethawong, C. Junbua, S. Chavadej, Photocatalytic H2 production from water splitting under visible light irradiation using Eosin Y-sensitized mesoporous-assembled Pt/TiO2 nanocrystal photocatalyst, Journal of power sources, 190 (2009) 513-524.

[34] N. Strataki, V. Bekiari, D.I. Kondarides, P. Lianos, Hydrogen production by photocatalytic alcohol reforming employing highly efficient nanocrystalline titania films, Applied Catalysis B: Environmental, 77 (2007) 184-189.

[35] C. Pojanavaraphan, A. Luengnaruemitchai, E. Gulari, Effect of support composition and metal loading on Au catalyst activity in steam reforming of methanol, International journal of hydrogen energy, 37 (2012) 14072-14084.

[36] W. Wu, L. Wen, L. Shen, R. Liang, R. Yuan, L. Wu, A new insight into the photocatalytic reduction of 4-nitroaniline to p-phenylenediamine in the presence of alcohols, Applied Catalysis B: Environmental, 130 (2013) 163-167.

[37] M. Nasr, R. Viter, C. Eid, R. Habchi, P. Miele, M. Bechelany, Enhanced photocatalytic performance of novel electrospun BN/TiO 2 composite nanofibers, New Journal of Chemistry, 41 (2017) 81-89.

[38] M. Nasr, L. Soussan, R. Viter, C. Eid, R. Habchi, P. Miele, M. Bechelany, High photodegradation and antibacterial activity of BN–Ag/TiO 2 composite nanofibers under visible light, New Journal of Chemistry, 42 (2018) 1250-1259.

[39] J. Rodríguez-Carvajal, FullProf, CEA/Saclay, France, (2001).

[40] L. Finger, D. Cox, A. Jephcoat, A correction for powder diffraction peak asymmetry due to axial divergence, Journal of applied Crystallography, 27 (1994) 892-900.

[41] A.A. Nada, M. Nasr, R. Viter, P. Miele, S.p. Roualdes, M. Bechelany, Mesoporous ZnFe2O4@ TiO2 nanofibers prepared by electrospinning coupled to PECVD as highly performing photocatalytic materials, The Journal of Physical Chemistry C, 121 (2017) 24669-24677.

[42] H. Song, H. Jiang, X. Liu, G. Meng, Efficient degradation of organic pollutant with WOx modified nano TiO2 under visible irradiation, Journal of Photochemistry and Photobiology A: Chemistry, 181 (2006) 421-428.

[43] J. Heyd, G.E. Scuseria, M. Ernzerhof, Hybrid functionals based on a screened Coulomb potential, The Journal of chemical physics, 118 (2003) 8207-8215.

[44] J. Heyd, J.E. Peralta, G.E. Scuseria, R.L. Martin, Energy band gaps and lattice parameters evaluated with the Heyd-Scuseria-Ernzerhof screened hybrid functional, The Journal of chemical physics, 123 (2005) 174101.

[45] P. Giannozzi, S. Baroni, N. Bonini, M. Calandra, R. Car, C. Cavazzoni, D. Ceresoli, G.L. Chiarotti, M. Cococcioni, I. Dabo, QUANTUM ESPRESSO: a modular and open-source software project for quantum simulations of materials, Journal of physics: Condensed matter, 21 (2009) 395502.

[46] N. Hirosaki, S. Ogata, C. Kocer, Ab initio calculation of the crystal structure of the lanthanide Ln2O3 sesquioxides, Journal of alloys and compounds, 351 (2003) 31-34.

[47] P.J. Hay, R.L. Martin, J. Uddin, G.E. Scuseria, Theoretical study of Ce O 2 and Ce 2 O 3 using a screened hybrid density functional, The Journal of chemical physics, 125 (2006) 034712.

[48] S.J. Doh, C. Kim, S.G. Lee, S.J. Lee, H. Kim, Development of photocatalytic TiO2 nanofibers by electrospinning and its application to degradation of dye pollutants, Journal of hazardous materials, 154 (2008) 118-127.

[49] R.D. Shannon, Revised effective ionic-radii and systematic studies of interatomic distances in halides and chalcogenides, Acta Crystallogr A, 32 (1976) 751-767.

[50] A. Jafari, S. Khademi, M. Farahmandjou, Nano-crystalline Ce-doped TiO2 powders: sol-gel synthesis and optoelectronic properties, Materials Research Express, 5 (2018) 095008.

[51] G. Li, L. Li, J. Boerio-Goates, B.F. Woodfield, High Purity Anatase TiO2 Nanocrystals: Near Room-Temperature Synthesis, Grain Growth Kinetics, and Surface Hydration Chemistry, Journal of the American Chemical Society, 127 (2005) 8659-8666.

[52] Y. Wang, L. Li, X. Huang, Q. Li, G. Li, New insights into fluorinated TiO2 (brookite, anatase and rutile) nanoparticles as efficient photocatalytic redox catalysts, RSC Advances, 5 (2015) 34302-34313.

[53] M. Šćepanović, M. Grujić-Brojčin, B. Abramović, A. Golubović, Structural, morphological, and optical study of titania-based nanopowders suitable for photocatalytic applications, Journal of Physics: Conference Series, IOP Publishing, 2017, pp. 012003.

[54] L. Thirugnanam, S. Kaveri, M. Dutta, N.V. Jaya, N. Fukata, Porous tubular rutile TiO2 nanofibers: synthesis, characterization and photocatalytic properties, Journal of nanoscience and nanotechnology, 14 (2014) 3034-3040.

[55] Y. Shi, C. Hamsen, X. Jia, K.K. Kim, A. Reina, M. Hofmann, A.L. Hsu, K. Zhang, H. Li, Z.-Y. Juang, Synthesis of few-layer hexagonal boron nitride thin film by chemical vapor deposition, Nano letters, 10 (2010) 4134-4139.

[56] V. Yadav, V. Kulshrestha, Boron nitride: a promising material for proton exchange membranes for energy applications, Nanoscale, 11 (2019) 12755-12773.

[57] S.M. Adyani, M. Ghorbani, A comparative study of physicochemical and photocatalytic properties of visible light responsive Fe, Gd and P single and tri-doped TiO2 nanomaterials, Journal of Rare Earths, 36 (2018) 72-85.

[58] R. Ma, M. Jahurul Islam, D. Amaranatha Reddy, T.K. Kim, Transformation of CeO2 into a mixed phase CeO2/Ce2O3 nanohybrid by liquid phase pulsed laser ablation for enhanced photocatalytic activity through Z-scheme pattern, Ceramics International, 42 (2016) 18495-18502.

[59] P. Zhou, Y. Xie, L. Liu, J. Song, T. Chen, Y. Ling, Bicrystalline TiO 2 heterojunction for enhanced organic photodegradation: engineering and exploring surface chemistry, RSC advances, 7 (2017) 16484-16493.

[60] C. Shen, K. Pang, L. Du, G. Luo, Green synthesis and enhanced photocatalytic activity of Ce-doped TiO2 nanoparticles supported on porous glass, Particuology, 34 (2017) 103-109.

[61] B. Bharti, S. Kumar, H.-N. Lee, R. Kumar, Formation of oxygen vacancies and Ti 3+ state in TiO 2 thin film and enhanced optical properties by air plasma treatment, Scientific reports, 6 (2016) 1-12.

[62] J. Zhang, H. Wong, D. Yu, K. Kakushima, H. Iwai, X-ray photoelectron spectroscopy study of high-k CeO2/La2O3 stacked dielectrics, AIP Advances, 4 (2014) 117117.

[63] K.I. Maslakov, Y.A. Teterin, M.V. Ryzhkov, A.J. Popel, A.Y. Teterin, K.E. Ivanov, S.N. Kalmykov, V.G. Petrov, P.K. Petrov, I. Farnan, The electronic structure and the nature of the chemical bond in CeO 2, Physical Chemistry Chemical Physics, 20 (2018) 16167-16175.

[64] S. Uppal, A. Arora, S. Gautam, S. Singh, R. Choudhary, S. Mehta, Magnetically retrievable Ce-doped Fe 3 O 4 nanoparticles as scaffolds for the removal of azo dyes, RSC advances, 9 (2019) 23129-23141.

[65] M. Ren, K. Qian, W. Huang, Electronic Metal-Support Interaction-Modified Structures and Catalytic Activity of CeOx Overlayers in CeOx/Ag Inverse Catalysts, Chemistry–A European Journal, 25 (2019) 15978-15982.

[66] K. Qian, H. Duan, Y. Li, W. Huang, Electronic Oxide–Metal Strong Interaction (EOMSI), Chemistry–A European Journal, 26 (2020) 13538-13542.

[67] Y. Li, Y. Zhang, K. Qian, W. Huang, Metal–Support Interactions in Metal/Oxide Catalysts and Oxide–Metal Interactions in Oxide/Metal Inverse Catalysts, ACS Catalysis, 12 (2022) 1268-1287.

[68] I. Nakamura, N. Negishi, S. Kutsuna, T. Ihara, S. Sugihara, K. Takeuchi, Role of oxygen vacancy in the plasma-treated TiO2 photocatalyst with visible light activity for NO removal, Journal of Molecular Catalysis A: Chemical, 161 (2000) 205-212.

[69] N. Li, X. Zou, M. Liu, L. Wei, Q. Shen, R. Bibi, C. Xu, Q. Ma, J. Zhou, Enhanced visible light photocatalytic hydrogenation of CO2 into methane over a Pd/Ce-TiO2 nanocomposition, The Journal of Physical Chemistry C, 121 (2017) 25795-25804.

[70] M. Saif, S. El-Molla, S. Aboul-Fotouh, M. Ibrahim, L. Ismail, D.C. Dahn, Nanostructured Gd3+-TiO2 surfaces for self-cleaning application, Journal of Molecular Structure, 1067 (2014) 120-126.

[71] M. Baitimirova, R. Viter, J. Andzane, A. van der Lee, D. Voiry, I. Iatsunskyi, E. Coy, L. Mikoliunaite, S. Tumenas, K. Załęski, Tuning of structural and optical properties of graphene/ZnO nanolaminates, The Journal of Physical Chemistry C, 120 (2016) 23716-23725.

[72] M. Pelaez, N.T. Nolan, S.C. Pillai, M.K. Seery, P. Falaras, A.G. Kontos, P.S. Dunlop, J.W. Hamilton, J.A. Byrne, K. O'shea, A review on the visible light active titanium dioxide photocatalysts for environmental applications, Applied Catalysis B: Environmental, 125 (2012) 331-349.

[73] M. Myilsamy, V. Murugesan, M. Mahalakshmi, Indium and cerium co-doped mesoporous TiO2 nanocomposites with enhanced visible light photocatalytic activity, Applied Catalysis A: General, 492 (2015) 212-222.

[74] J. Dhanalakshmi, S. Iyyapushpam, S. Nishanthi, M. Malligavathy, D.P. Padiyan, Investigation of oxygen vacancies in Ce coupled TiO2 nanocomposites by Raman and PL spectra, Advances in Natural Sciences: Nanoscience and Nanotechnology, 8 (2017) 015015.

[75] M. Thiruppathi, P.S. Kumar, P. Devendran, C. Ramalingan, M. Swaminathan, E. Nagarajan, Ce@ TiO2 nanocomposites: An efficient, stable and affordable photocatalyst for the photodegradation of diclofenac sodium, Journal of Alloys and Compounds, 735 (2018) 728-734.

[76] N. Ahmadi, A. Nemati, M. Bagherzadeh, Synthesis and properties of Ce-doped TiO2-reduced graphene oxide nanocomposite, Journal of Alloys and Compounds, 742 (2018) 986-995.

[77] M. Nasr, A. Abou Chaaya, N. Abboud, M. Bechelany, R. Viter, C. Eid, A. Khoury, P. Miele, Photoluminescence: A very sensitive tool to detect the presence of anatase in rutile phase electrospun TiO2 nanofibers, Superlattices and Microstructures, 77 (2015) 18-24.

[78] E. Borgarello, J. Kiwi, M. Graetzel, E. Pelizzetti, M. Visca, Visible light induced water cleavage in colloidal solutions of chromium-doped titanium dioxide particles, Journal of the American Chemical Society, 104 (1982) 2996-3002.

[79] Z. Liu, Q. Wang, X. Tan, S. Zheng, H. Zhang, Y. Wang, S. Gao, Solvothermal preparation of Bi/Bi2O3 nanoparticles on TiO2 NTs for the enhanced photoelectrocatalytic degradation of pollutants, Journal of Alloys and Compounds, 815 (2020) 152478.

[80] K.R. Diab, H.H. El-Maghrabi, A.A. Nada, A.M. Youssef, A. Hamdy, S. Roualdes, S. Abd El-Wahab, Facile fabrication of NiTiO3/graphene nanocomposites for photocatalytic hydrogen generation, Journal of Photochemistry and Photobiology A: Chemistry, 365 (2018) 86-93.

[81] A. Barhoum, H.H. El-Maghrabi, I. Iatsunskyi, E. Coy, A. Renard, C. Salameh, M. Weber, S. Sayegh, A.A. Nada, S. Roualdes, Atomic layer deposition of Pd nanoparticles on self-supported carbon-Ni/NiO-Pd nanofiber electrodes for electrochemical hydrogen and oxygen evolution reactions, Journal of colloid and interface science, 569 (2020) 286-297.

[82] H.H. El-Maghrabi, A.A. Nada, M.F. Bekheet, S. Roualdes, W. Riedel, I. Iatsunskyi, E. Coy, A. Gurlo, M. Bechelany, Coaxial nanofibers of nickel/gadolinium oxide/nickel oxide as highly effective electrocatalysts for hydrogen evolution reaction, Journal of Colloid and Interface Science, 587 (2021) 457-466.

[83] H.A. Yurtsever, M. Çiftçioğlu, Photocatalytic hydrogen production with erbium doped Titania powders, J. Eng. Fundam., 2 (2015) 26-37.

[84] Y. Liu, L. Xie, Y. Li, J. Qu, J. Zheng, X. Li, Photocatalytic Hydrogen Generation Over Lanthanum Doped TiO2 Under UV Light Irradiation, Journal of nanoscience and nanotechnology, 9 (2009) 1514-1517.
[85] N. Vinothkumar, M. De, Enhanced photocatalytic hydrogen production from water–methanol mixture using cerium and nonmetals (B/C/N/S) co-doped titanium dioxide, Materials for Renewable and Sustainable Energy, 3 (2014) 25.
[86] N. Li, H. Huang, R. Bibi, Q. Shen, R. Ngulube, J. Zhou, M. Liu, Noble-metal-free MOF derived hollow CdS/TiO2 decorated with NiS cocatalyst for efficient photocatalytic hydrogen evolution, Applied Surface Science, 476 (2019) 378-386.
[87] K. Kordek, H. Yin, P. Rutkowski, H. Zhao, Cobalt-based composite films on electrochemically activated carbon cloth as high performance overall water splitting electrodes, International Journal of Hydrogen Energy, 44 (2019) 23-33.
[88] K.K. Mandari, A.K.R. Police, J.Y. Do, M. Kang, C. Byon, Rare earth metal Gd influenced defect sites in N doped TiO2: defect mediated improved charge transfer for enhanced photocatalytic hydrogen production, International Journal of Hydrogen Energy, 43 (2018) 2073-2082.
[89] Y.-G. Yu, G. Chen, X.-K. Yang, Y.-S. Zhou, Z.-H. Han, A red La (OH) 3/TiO2: B, N composite photocatalyst for broad-band visible-light-driven hydrogen evolution, International journal of hydrogen energy, 39 (2014) 13534-13542.
[90] A.A. Chilkalwar, S.S. Rayalu, Synergistic plasmonic and upconversion effect of the (Yb, Er) NYF-TiO2/Au composite for photocatalytic hydrogen generation, The Journal of Physical Chemistry C, 122 (2018) 26307-26314.
[91] C. HUANG, Y. Wansheng, D. Liqin, L. Zhibin, S. Zhengang, L. ZHANG, Effect of Nd3+ doping on photocatalytic activity of TiO2 nanoparticles for water decomposition to hydrogen, Chinese Journal of Catalysis, 27 (2006) 203-209.
[92] N. Khalid, M. Liaqat, M.B. Tahir, G. Nabi, T. Iqbal, N. Niaz, The role of graphene and europium on TiO2 performance for photocatalytic hydrogen evolution, Ceramics International, 44 (2018) 546-549.
[93] X. Fan, J. Wan, E. Liu, L. Sun, Y. Hu, H. Li, X. Hu, J. Fan, High-efficiency photoelectrocatalytic hydrogen generation enabled by Ag deposited and Ce doped TiO2 nanotube arrays, Ceramics International, 41 (2015) 5107-5116.
[94] J. Jin, C. Wang, X.-N. Ren, S.-Z. Huang, M. Wu, L.-H. Chen, T. Hasan, B.-J. Wang, Y. Li, B.-L. Su, Anchoring ultrafine metallic and oxidized Pt nanoclusters on yolk-shell TiO2 for unprecedentedly high photocatalytic hydrogen production, Nano Energy, 38 (2017) 118-126.
[95] S. Peng, Y. Huang, Y. Li, Rare earth doped TiO2-CdS and TiO2-CdS composites with improvement of photocatalytic hydrogen evolution under visible light irradiation, Materials Science in Semiconductor Processing, 16 (2013) 62-69.
[96] C.H. Ravikumar, M. Sakar, A. Mahto, R.T. Nanjundaiah, R. Thippeswamy, S.R. Teixeira, R.G. Balakrishna, Observation of oxo-bridged yttrium in TiO2 nanostructures and their enhanced photocatalytic hydrogen generation under UV/Visible light irradiations, Materials Research Bulletin, 104 (2018) 212-219.
[97] J. Buckeridge, K.T. Butler, C.R.A. Catlow, A.J. Logsdail, D.O. Scanlon, S.A. Shevlin, S.M. Woodley, A.A. Sokol, A. Walsh, Polymorph engineering of TiO2: demonstrating how absolute reference potentials are determined by local coordination, Chemistry of Materials, 27 (2015) 3844-3851.
[98] K.-A.N. Duerloo, M.T. Ong, E.J. Reed, Intrinsic piezoelectricity in two-dimensional materials, The Journal of Physical Chemistry Letters, 3 (2012) 2871-2876.
[99] R.S. Dima, L. Phuthu, N.E. Maluta, J.K. Kirui, R.R. Maphanga, Electronic, Structural, and Optical Properties of Mono-Doped and Co-Doped (210) TiO2 Brookite Surfaces for Application in Dye-Sensitized Solar Cells—A First Principles Study, Materials, 14 (2021) 3918.
[100] J. Yu, J. Low, W. Xiao, P. Zhou, M. Jaroniec, Enhanced photocatalytic CO2-reduction activity of anatase TiO2 by coexposed {001} and {101} facets, Journal of the American Chemical Society, 136 (2014) 8839-8842.

[101] V. Štengl, J. Henych, M. Slušná, h-BN-TiO2 nanocomposite for photocatalytic applications, Journal of Nanomaterials, 2016 (2016).